

Lappeenranta University of Technology  
LUT School of Energy Systems  
Degree Program in Electrical Engineering

Iiro Pelli

**CAPACITIVE DISPLACEMENT SENSOR'S APPLICABILITY AND  
LIMITATIONS IN CONDITION MONITORING SYSTEMS OF  
ROTATING ELECTRICAL MACHINES.**

Examiners:

Professor Olli Pyrhönen  
D.Sc. Markku Niemelä

Supervisors:

M.Sc Olli Liukkonen



## **ABSTRACT**

Lappeenranta University of Technology  
LUT School of Energy Systems  
Degree Program in Electrical Engineering

Iiro Pelli

### **Capacitive Displacement Sensor's Applicability and Limitations in Condition Monitoring Systems of Rotating Electrical Machines.**

Master's Thesis

73 pages, 49 figures, 13 tables, 3 appendices

Examiners:            Professor Olli Pyrhönen  
                             D.Sc. Markku Niemelä

Supervisor:           M.Sc. Olli Liukkonen

Keywords: Condition, monitoring, electrical, machines, bearings, frequency, digital, circuit, sensor, capacitance, logic, controller.

Condition monitoring of electrical machines in industry is essential in maximizing production and upkeep. Condition monitoring applications use a vast variety of different tools that are used to prevent unexpected system shutdown. The tools consist generally of sensors, third party tools, data acquisition, signal processing and its visualization and analyzation.

Lappeenranta University of Technology has developed a capacitive displacement sensor for active magnetic bearing application. The purpose of this thesis is to find out how the sensor is applicable in condition monitoring of electrical machines. The goal of the thesis is to list the sensor's applicability, limitations, and its connectivity to external data acquisition computers as well as proposing potential future development. The sensor is also tested in practice by installing it on motor shaft so that potential known frequencies could be detected. The sensor is also connected to ABB's condition monitoring systems.

The sensor is able to detect motor shaft unbalance at micrometer level and potentially the frequencies from the bearings in its closure. The connectivity to higher level computers is also proven to be effortless. It is also possible to further develop advanced signal processing algorithms on the sensor's digital circuit.

# TABLE OF CONTENTS

<b>1</b>	<b>INTRODUCTION .....</b>	<b>6</b>
1.1	GOALS AND DELIMITATIONS .....	7
1.2	OUTLINE OF THE THESIS .....	7
<b>2</b>	<b>CONDITION MONITORING IN ELECTRICAL MACHINES .....</b>	<b>8</b>
2.1	TYPES OF SENSORS USED IN CONDITION MONITORING .....	9
2.1.1	<i>Vibration sensors</i> .....	9
2.1.2	<i>Temperature sensors</i> .....	12
2.1.3	<i>Voltage and current sensors</i> .....	12
2.1.4	<i>Acoustic sensors</i> .....	12
2.2	GENERAL INDUCTION MOTOR FAULTS .....	12
2.2.1	<i>Rotor faults</i> .....	13
2.2.2	<i>Stator faults</i> .....	14
2.2.3	<i>Rolling element bearing faults</i> .....	14
2.2.4	<i>Sleeve bearing faults</i> .....	16
2.3	DATA ACQUISITION .....	17
2.4	SIGNAL ANALYSIS .....	18
<b>3</b>	<b>LUT CAPACITIVE DISPLACEMENT SENSOR.....</b>	<b>22</b>
3.1	OVERVIEW .....	22
3.1.1	<i>Technical specifications</i> .....	24
3.2	CORRESPONDENCE TO MEASUREMENT STANDARDS .....	26
3.3	MODIFICATION POSSIBILITIES .....	27
3.3.1	<i>Tuning the on-board A/D converter</i> .....	27
3.3.2	<i>Splitting the sensor apart</i> .....	28
3.3.3	<i>Slave controller</i> .....	29
3.3.4	<i>Additional sensors</i> .....	32
3.3.5	<i>Additional output links</i> .....	35
3.4	FPGA LOGIC .....	36
3.4.1	<i>Digital filtering</i> .....	37
3.4.2	<i>Programming the chip</i> .....	41
3.4.3	<i>Data storage</i> .....	43
3.5	CALCULATION PLATFORM COMPARISON .....	43
3.5.1	<i>On an industrial PC</i> .....	43
3.5.2	<i>On the capacitive sensor</i> .....	44
3.6	COMMISSIONING ON THE MACHINE .....	44

3.6.1	<i>Inside the motor frame</i> .....	45
3.6.2	<i>Outside the motor frame</i> .....	46
3.6.3	<i>Mounting on drive-end</i> .....	47
3.6.4	<i>Mounting on non-drive-end</i> .....	47
3.7	CONNECTIVITY .....	47
3.7.1	<i>ABB AC500-CMS PLC</i> .....	48
3.7.2	<i>Other computers</i> .....	52
3.7.3	<i>Master topology</i> .....	52
<b>4</b>	<b>LABORATORY TEST-SETUP</b> .....	<b>54</b>
4.1	CONCURRENT USE OF TWO SENSORS .....	62
<b>5</b>	<b>ABB PRACTICAL DEMONSTRATION</b> .....	<b>64</b>
<b>6</b>	<b>SUMMARY AND CONCLUSIONS</b> .....	<b>68</b>
	<b>REFERENCES</b> .....	<b>69</b>

## **APPENDIX**

- I** Model parameters of a System Generator CIC-filter
- II** Matlab digital filter design code
- III** Matlab code used in Fast-Fourier Transform

## LIST OF SYMBOLS AND ABBREVIATIONS

A/D	Analog to Digital
AC	Alternating Current
ADC	Analog to Digital Converter
AE	Acoustic Emission
ANN	Artificial Neural Network
API	American Petroleum Institute
ASIC	Application-Specific Integrated Circuit
BD	Ball Diameter
BPM	Ball Pass Frequency on Inner Race
BPO	Ball Pass Frequency on Outer Race
BRAM	Block Random-Access Memory
CM	Condition Monitoring
CMOS	Complementary Metal-Oxide Semiconductor
CPM	Cycles per Minute
CPU	Central Processing Unit
DAQ	Data Acquisition
DC	Direct Current
DFT	Discrete Fourier Transform
DR	Data Rate
DRAM	Dynamic Random-Access Memory
EMI	Electromagnetic Interference
EoE	Ethernet over EtherCAT
EPRI	Electric Power Research Institute
EtherCAT	Ethernet for Control Automation Technology
EEPROM	Electrically Erasable Programmable Read-Only Memory
FEM	Finite Element Method
FFT	Fast-Fourier Transform
FIR	Finite Impulse Response
FPGA	Field-Programmable Gate Array
FTF	Fundamental Train Frequency
HVAC	Heating, Ventilation and Air Conditioning
IEEE	Institute of Electronics and Electrical Engineers
IGBT	Insulated-Gate Bipolar Transistor
IIR	Infinite Impulse Response
IoT	Internet of Things
LPF	Low-pass Filter
LSB	Least Significant Bit
MCSA	Machine Current Signature Analysis
MEMS	Microelectromechanical Systems
ML	Machine Learning
NB	Number of Balls

OSR	Decimation Ratio
PCB	Printed Circuit Board
PD	Pitch Diameter
PdM	Predictive Maintenance
PLC	Programmable Logic Controller
PM	Preventive Maintenance
ProM	Proactive Maintenance
PWM	Pulse Width Modulation
ReM	Reactive Maintenance
RF	Radio Frequency
RMS	Root-Mean-Square
RPM	Rounds per Minute
RTD	Resistance Temperature Detector
SNR	Signal to Noise Ratio
SPI	Serial Peripheral Interface
SPV	Shock Pulse Value
UMP	Unbalanced Magnetic Pull
VFD	Variable Frequency Drive
VSD	Variable Speed Drive
WLAN	Wireless Local Area Network

$A$	Surface area
$a$	Acceleration
$B$	Bandwidth
$C$	Capacitance
$d$	Diameter
$f$	Frequency
$f_{\text{CLK}}$	Clock frequency
$f_{\text{MCLK}}$	Master clock frequency
$f_{\text{N}}$	Nyquist frequency
$f_{\text{n}}$	Natural frequency
$f_{\text{res}}$	Resonance frequency
$f_{\text{s}}$	Sampling frequency
$I$	Electrical current
$k$	Shaft stiffness
$L$	Inductance
$m$	Mass
$P_{\text{e}}$	Electrical power
$T_{\text{m}}$	Mechanical torque
$U$	Voltage
$v$	Velocity
$x$	Displacement
$\bar{x}_n$	Average value over $n$ samples

$\varepsilon$	Permittivity
$\omega$	Angular rotational speed
$\phi$	Contact angle

# 1 INTRODUCTION

Every industrial machine degrades over time and requires periodic maintenance. Usually, without advanced tools, the degradation is noticed when the system performance has dropped significantly until it becomes human sensible. In these cases, the damages are often severe to cause large system damage and long-term downtime and costs due to error tracing and component replacements. Condition monitoring (CM) stands for continuous tracking of process parameters to gain preemptive information about degrading components before they cause major damage to the system. CM improves machine life, efficiency and uptime, reduces maintenance costs and prevents unexpected motor failure (SKF, 2015). In case of electrical machines, the parameters under observations are often vibration, temperature, acoustic noise and electrical current, depending on the application. The data analysis can be done a few times per year on-site using handheld devices or continuously by local computers or remotely over internet using companies' own cloud computing services.

In electrical machines, bearings are one of the major causes of malfunctioning systems, and some research shows that the bearings are the problem source of over 40 % of cases (Han & Song, 2003). Aside from natural wear, further damage on bearings is frequently caused by current leakages, inaccurate installations, improper bearing lubricants, stator and rotor faults, and so on. A damaged component produces added vibration to the machine, which is commonly detected by using an external accelerometer installed on a motor frame. Since different machine components produce unique frequencies to the system, by performing mathematical study and examination on the data, such as spectral analysis, pinpointing an individual component for faulty performance becomes possible.

Lappeenranta University of Technology in collaboration with ABB Finland has developed a modern capacitive position displacement sensor that currently can measure radial shaft displacement at micrometer level. It measures the distance by using information from four different capacitive plates positioned around a shaft and therefore enhances the measurement accuracy due to an averaging effect of the large capacitive surface. The sensor costs a fraction of currently available industrial high precision probes' prices. It is possible to be modified to support additional sensors as the sensor is still in development phase. It also has potential to contribute to Industrial Internet of Things (IIoT), which is continuously finding more and more research areas in modern industry. Because of the sensor's inexpensiveness and modularity, ABB Finland has shown their interest in using the sensor in their condition monitoring applications. This thesis's purpose is to address what the sensor is currently capable of, how the sensor can be modified to meet ABB's needs and how it can be commissioned to rotating machines as well as connected to existing ABB condition monitoring solutions.

## **1.1 Goals and delimitations**

ABB Finland have shown their interest to connect the LUT capacitive sensor to their own CM services along with a few new features. Some of these features are additional sensors, possible splitting of the sensor, signal processing platform topology examination and modification of connectivity. The goal of this thesis is to discover if these features are possible to be implemented and if so, how. Additionally, optimal installation to motors and connectivity to CM services is an essential topic. Finally, a practical CM presentation using the sensor is planned at ABB laboratory at Pitäjänmäki, Helsinki.

## **1.2 Outline of the thesis**

The second chapter discusses condition monitoring, including electrical machine fault sources, their causes and their effects on the machine. The chapter introduces the reader to the topic of CM in general, firstly by presenting some typical technologies used in condition monitoring of rotating machinery. The chapter covers things such as what typical sensors, common faults in machines and analysis techniques used in industry are.

The third chapter goes through the capacitive sensor. The sensor's layout, functionality and modification possibilities are presented and discussed. Sensor's mounting position to electric motors is analyzed. Connectivity to ABB's intelligent machines is examined and alternatives are presented and compared with each other. Additionally, as the laboratory and industrial surroundings are dynamic and highly hardware dependent, it is examined on which platform it would be smartest to do signal processing. Some algorithm ideas are also presented.

Chapter four presents different laboratory setups and achieved results. The results are analyzed, and some comparison is done to pre-existing data to distinguish possible machine faults.

Chapter five presents the laboratory demonstration at Pitäjänmäki, Helsinki. The results are analyzed and compared if some faults are detected similarly as in the previous laboratory environment.

Chapter six contains summation of this thesis including conclusions, ideas and proposals for future work.

## 2 CONDITION MONITORING IN ELECTRICAL MACHINES

Condition monitoring extends system life and improves machine efficiency. Degraded machine components increase power losses and result in undesired system functionality, and in the worst cases, in accidental system halts. CM aims to prematurely gather and diagnose system data for eccentric performance before permanent damage has been developed.

Four basic principles exist for CM maintenance. In reactive maintenance (ReM) the system is not repaired until it is damaged completely. Preventive maintenance (PM) improves this by repairing the machine before a breakdown. Additionally, predictive maintenance (PdM) uses statistical information and trends to perform maintenance at the best suitable time. Finally, proactive maintenance (ProM) attempts to improve the system life by performing maintenance directly at the root causes (Stamboliska, 2015). CM systems generally consist of transduction, data acquisition, signal processing and diagnostics which is later used in maintenance planning as seen in figure 1.

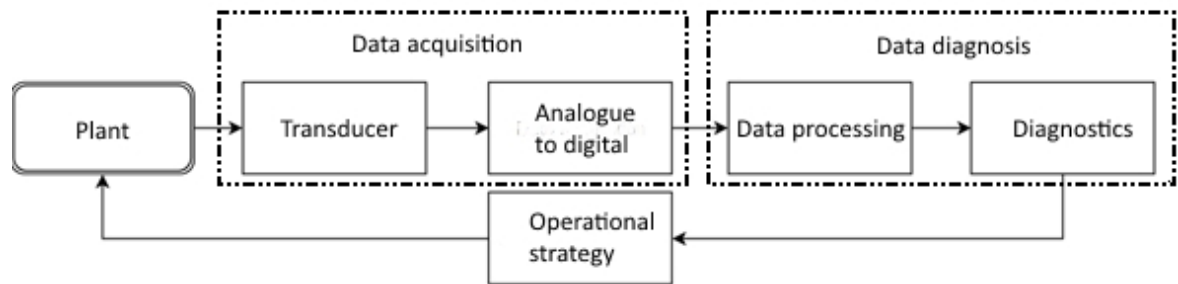


**Figure 2.1.** General simplified step-by-step flow chart of condition monitoring systems.

The data acquisition stands for converting analogue signal into digitally processable digital form, which is done using analogue to digital (A/D) converters. The process should be implemented so that the acquired data is as noise-free and accurate as possible. The data acquisition task's implementation greatly depends on the system complexity: amount of signal inputs, desired signal processing algorithms, data rates, distances, computational power, hardware limitations, and so on. Therefore, thorough planning is required to determine if the acquisition task should be separated from the processing and diagnostic tasks as well as if the monitoring should be done periodically, continuously or in real-time and whether it is done off-line or on-line. Off-line monitoring stands for measurement when the system is on halt, and on-line is performed while the system is running.

The periodical monitoring plan aims to execute inspections on the system on predetermined time intervals. In continuous monitoring, a sensor is usually installed on the machine to act without supervision. This requires the system to be disassembled which increases system downtime. Continuous monitoring method can detect faults immediately as well as can form trends meanwhile. The method also reduces human labor and enables safe monitoring in

hazardous areas. However, implementation of continuous monitoring is often more expensive than the use of periodical monitoring (Lindh, 2003).

Continuous off-line monitoring collects data and stores it on the measuring device's memory chip. Additionally, on-line continuous monitoring system collects data continuously and sends it to a host computer that processes the data further. The data can be preprocessed, lessening the requirement of the link speeds between computer and the device as the communication can consist only of alarms or fault alerts, or processed on the host computer, which lessens the computational requirements of the sensor but increases the link speed necessities due to high amount of measurement samples.

Periodical monitoring is always done by humans and might thus also contain human error, but also enables on-site human sense analysis. Periodical monitoring also enables the maintenance of the machine when the measurement work is done (Lindh, 2003).

Data acquisition is done using either data acquisition cards (DAQ) or boards, separated or embedded into a monitoring system. As the industrial environment might contain electromagnetic interference (EMI) and other sources of interference, cable management, choices and shielding play an important role at keeping the signals consistent when transferring data between two platforms. Additionally, since the data processing can nowadays be done using powerful cloud computing, connectivity to internet is also a thing to note.

## **2.1 TYPES OF SENSORS USED IN CONDITION MONITORING**

In the case of rotating machines regardless of their size and rotating speed, often the parameters under observation are

- vibration,
- temperature,
- acoustic noise,
- electrical current,
- voltage.

### **2.1.1 *Vibration sensors***

Vibration sensors are based on detecting displacement in time domain or any of its time derivatives. The vibration can be sensed by measuring the displacement, acceleration or speed in x- and y-coordinates. The peak-to-peak values are used to identify the severity of machine damage. Accelerometers are typically the most popular choice due to their small size, and their natural frequencies of miniature accelerometers can reach up to 200 kHz. The natural frequencies are designed so that generally from near DC frequencies to 30 % of the available bandwidth is used, at maximum. A typical frequency response of an accelerometer is shown below. It is seen that the attenuation increases as the frequencies decrease.

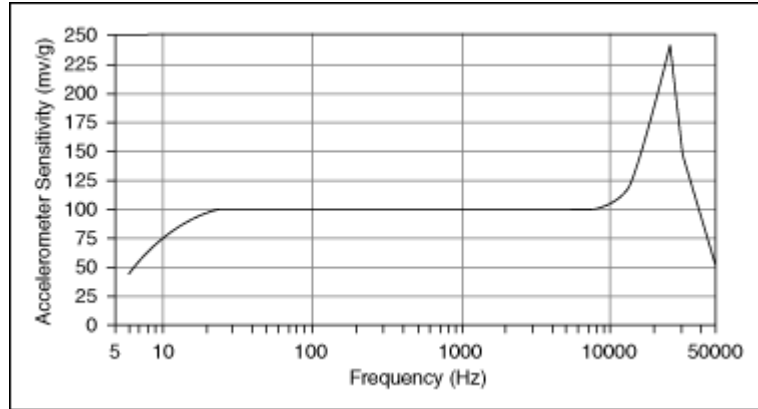


**Figure 2.2.** Frequency response of a typical accelerometer (National Instruments).

Generally, accelerometers are used to sense bearing housing’s acceleration, but speed and displacement is also possible to approximate by integrating the acceleration signal, since speed  $v$  is the first and acceleration  $a$  is the second derivative of displacement  $x$

$$\frac{dx}{dt} = v; \frac{d^2x}{dt^2} = a, \quad (1.1)$$

and

$$v = \int a \, dt; x = \int v \, dt. \quad (1.2)$$

The mathematical integration is also less prone to interference and improves signal-to-noise ratio (SNR), whereas estimating higher derivatives using differentiation degrades the SNR unless the differentiation algorithm is optimized for each application, for example by using signal smoothing techniques.

Piezoelectric accelerometers are used in industry since they have wide bandwidth and frequency response as well as high SNR. AC type accelerometers are used for dynamic testing whereas DC types, such as MEMS and piezoresistive sensors can measure static acceleration, such as gravity, down to 0 Hz in theory. Low frequency sensors are required especially in low-speed machinery as their frequency bandwidth is generally low (0,1-10 Hz) (Stamboliska, 2015).

Eddy current probes and induction sensors are the most popular noncontact probes used in detecting displacement. They are based on mechanical and electrical runout, which stands for displacement of rotor shaft’s eccentricity and rotor’s varying conductivity due to surface imperfections, respectively. Other popular displacement sensors used are based on capacitive, laser, confocal and ultrasonic quantities. The decision of sensor type is highly dependent on the observable phenomena and machine’s rotating speed. As the vibrational frequencies increase, the absolute values of displacement lessen but their acceleration increases (Tavner, 2008). Displacement sensors are generally used in 0-100 Hz range, velocity sensors for 10-1kHz and accelerometers for speeds above 1 kHz. (Stamboliska, 2015) also presents a following figure as a general guideline for choosing a sensor depending

on the machine rotating speed. It shows that choosing a displacement sensor is better for lower frequencies whereas accelerometer is a better choice for higher frequencies.

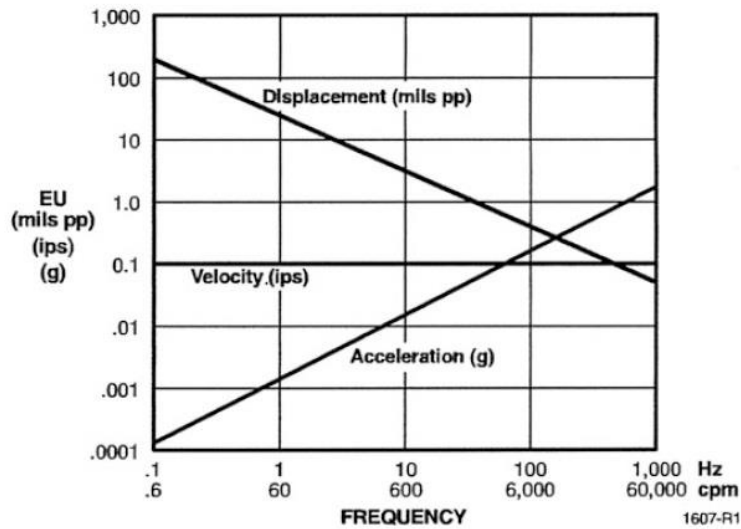


**Figure 2.3.** Guideline for selecting a sensor according to machine’s rotating speed. Mils are the thousandths of an inch, pp denotes peak-to-peak displacement, ips is inches per second, g is grams and cpm stands for “cycles per minute” (Stamboliska, 2015).

Typically, the vibration sensors are installed on the machine frame or bearing housing since they need to be physically mounted on the target. Usually two separate sensors are used to measure radial X and Y displacements individually. Multi-coordinate X and Y axis measurement also enables the calculation of vibration difference between shaft ends, which is achieved by using two sensors mounted on opposite shaft ends. The sensors are standardly mounted on 90° angle in respect to each other as seen in figure 2.4.

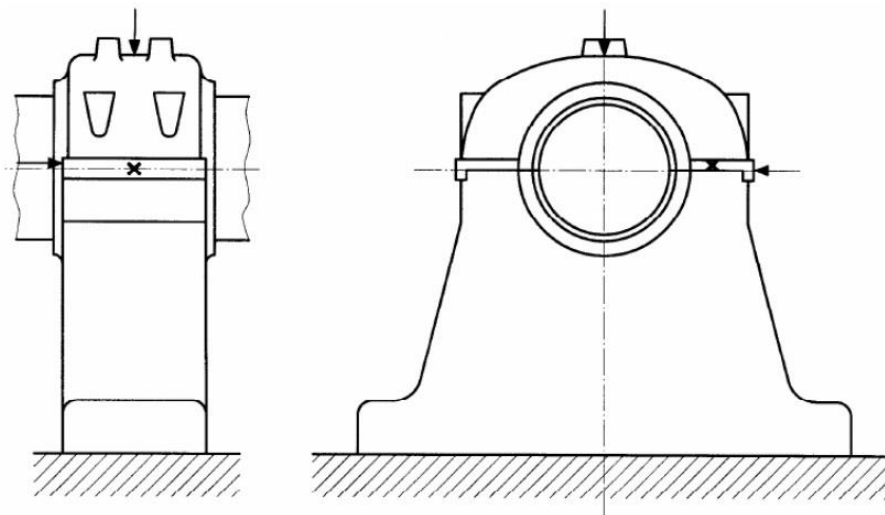


**Figure 2.4.** Vibration measuring points for pedestal bearings (ISO 10816-1).

However, the physical mounting requirement can also be their disadvantage since they can only be installed on solid, stationary platforms, such as motor frames or bearing housings. If a transducer is installed on the frame and the measurement target is the motor shaft, the achieved measurements are relative to the motor frame itself and contain the motor frame resonance frequencies as well as error from other sources and therefore will not necessarily produce completely reliable results. In other words, a noncontact sensor, such as an eddy current sensor or a capacitive sensor, is required to measure shaft's vibration without the machine noise since the axis surface is constantly in rotating movement. Exact results are achievable by mounting the sensor on a rigid frame, e.g. on a support platform next to the motor (Rao, 2000).

### ***2.1.2 Temperature sensors***

Stator winding and bearing temperatures are typically measured using resistance temperature detectors (RTDs), for which PT100 is one of the most popular choices. The increased temperatures are an indicator of e.g. degrading cooling system or circulating currents. Overheating may be caused by overcurrent and overvoltage by faulty power supply or modulation and stator insulation faults. Additionally, bearing misalignment causes extra physical stress on ball bearings which increases friction, improper lubrication, bearing overload and bearing temperatures.

### ***2.1.3 Voltage and current sensors***

Stator currents and voltages can be measured using multimeters and probes, and possibly estimated by sensors of variable speed drives (VSD). Faults, such as stator defects, are commonly detected using stator current signal analysis.

### ***2.1.4 Acoustic sensors***

Acoustic sensors are based on detecting acoustic emission (AE) from bearings using microphones that listen to high frequency sound waves that origin from solids as they undergo a crack or deformation. For example, bearings produce AE when circulating currents inflict physical damage e.g. microcraters on the outer ring's surface. AE's frequency ranges are in the ultrasonic range, due to which traditional microphones are not used. AE is helpful in detecting faults at extremely early stages and PM strategies.

## **2.2 GENERAL INDUCTION MOTOR FAULTS**

Different machine parts produce characteristic frequencies to the system that can be identified. Different vibrations are typically the outcomes of an unbalanced rotor, misaligned rotor shafts, gearboxes, loose shafts in bearing housings, oil whirl and whip in sleeve bearings and additionally of different rolling bearing elements. The faults can be classified in three different categories:

- Electrical faults: Faults due to electrical functions of the machine such as unbalanced supply voltage or current, under or overvoltage or current, reverse phase sequence, earth fault, overload, stator winding short-circuit and crawling.
- Mechanical faults: Rotor faults such as unbalance, shaft or bearing misalignment, bearing damage, air-gap eccentricity and stator winding failure.
- Environmental faults: Chemical substances such as gases corroding the machine, as well as ambient temperatures and moisture (Karmakar, 2016).

IEEE and Electric Power Research Institute (EPRI) have researched the occurrence of different induction motor faults (table 1).

**Table 1.** Typical induction motor fault occurrences gathered by IEEE and EPRI (Karmakar, 2016).

Researcher	Bearing faults [%]	Stator faults [%]	Rotor faults [%]	Other faults [%]
IEEE	42	28	8	22
EPRI	41	36	9	14

The different faults have been vastly studied, and it is noted that the resulting vibrational frequencies from stator and rotor faults are often harmonic multiplies of the motor rotational frequency  $f_{rot}$  as in the following equation

$$f_h = f_{rot} \pm k f_{rot}, \quad (2)$$

where  $f_h$  is the harmonic frequency in hertz and  $k$  is an integer (Tavner, 1987). For example, for a 1500 rpm induction motor, the vibrational rotor frequencies are roughly 25, 50, 75 and 100 Hz, and can be detected as anomalies in spectral analysis using FFT. The bearings produce distinct characteristic frequencies typical to their complex assembly parts' geometries, which are presented later below.

### 2.2.1 Rotor faults

Typical induction motor rotor faults are broken bars and cracked rotor end-rings. Additionally, rotor mass unbalance is a common phenomenon and exists always at some degree due to nonidealities (Rao, 2000). Unbalance generates additional radial force that acts between the rotating shaft and stationary structure like bearing housing or machine frame. This radial force causes additional stress and vibration to structure which may further lead to failure in bearings, for example. However, it may not always be a subject of concern until the unbalance begins to be massive enough to cause air-gap between rotor and stator to be nonuniform. This leads to motor's electromagnetic pull to differ at each rotor side and causes the rotor to move in the direction of the larger pull. In the most extreme rotor unbalance events, the rotor might grind against the stator surface resulting in physical wear and fast degradation. The rotor faults result in displacement and causes the torque to vary. The ideal motor's mechanical torque is proportional to the electrical current according to equation

$$T_m = P_e \omega = UI\omega, \quad (3)$$

where  $P_e$  is electrical power,  $U$  is voltage,  $I$  is electrical current and  $\omega$  is angular rotating speed. As the voltage and rotating speed is kept constant, the varying torque causes electrical current to alter. Therefore, rotor faults can be diagnosed by observing the electrical current. Motor current signature analysis (MCSA) is widely used technique in broken rotor bar identification applications due to its non-invasiveness, accuracy, cost effectiveness and on-line applicability.

Additionally, when a motor and load shafts are physically connected, a risk of angular and parallel misalignment is present (figure 2.5). In these cases, extra stress will effect on the bearings of both machines.

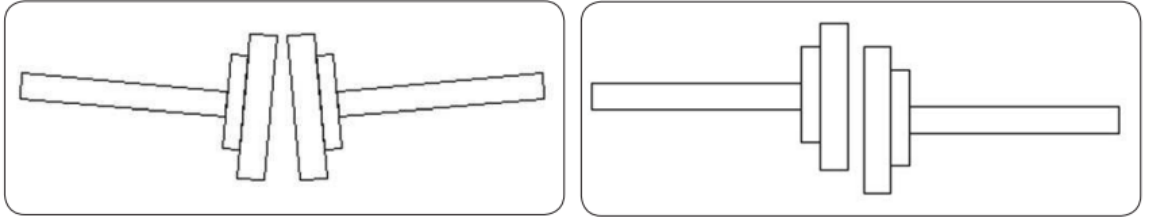


**Figure 2.5.** Angular shaft misalignment (left) and parallel shaft misalignment (right) (SKF).

### 2.2.2 Stator faults

Stator faults consist of asymmetry between stator windings and short-circuit of inter-turn winding cables due to cable insulation degradation. The asymmetry enables the machine to work but with reduced output torque whereas the short-circuit causes greater damage and eventually machine failure in shorter time. The shorted circuits result in increased electrical discharge activity which produce phenomena such as increased EMI, acoustic energy as well as increased temperatures. Stator current signal analysis has been used in distinguishing stator faults as the discharge activity causes variance in stator voltages and currents. Other methods, such as Canadian method and USA method, have also been used in identifying stator faults (Tavner, 1987).

### 2.2.3 Rolling element bearing faults

The rolling element bearings consist of roller elements, inner and outer race, bearing cage and bearing housing (figure 2.6). Each of these elements produce distinct separate characteristic frequencies to the machine equal to the following equations

fundamental train frequency

$$FTF = \frac{S}{2} \left(1 - \frac{BD}{PD} \cos\phi\right), \quad (4)$$

ball pass frequency on the inner race

$$BPFI = \frac{NB}{2} S \left( 1 + \frac{BD}{PD} \cos \phi \right) \quad (5)$$

ball spin frequency

$$BSF = \frac{PD}{2 \cdot BD} S \left[ 1 - \left( \frac{BD}{PD} \right)^2 \cos^2 \phi \right], \quad (6)$$

and ball pass frequency on the outer race

$$BPFO = \frac{NB}{2} S \left( 1 - \frac{BD}{PD} \cos \phi \right), \quad (7)$$

where  $PD$  is the pitch diameter,  $BD$  is ball diameter,  $\phi$  is ball or roller contact angle,  $NB$  is the number of balls and  $S$  is rotating speed in revolutions per second.

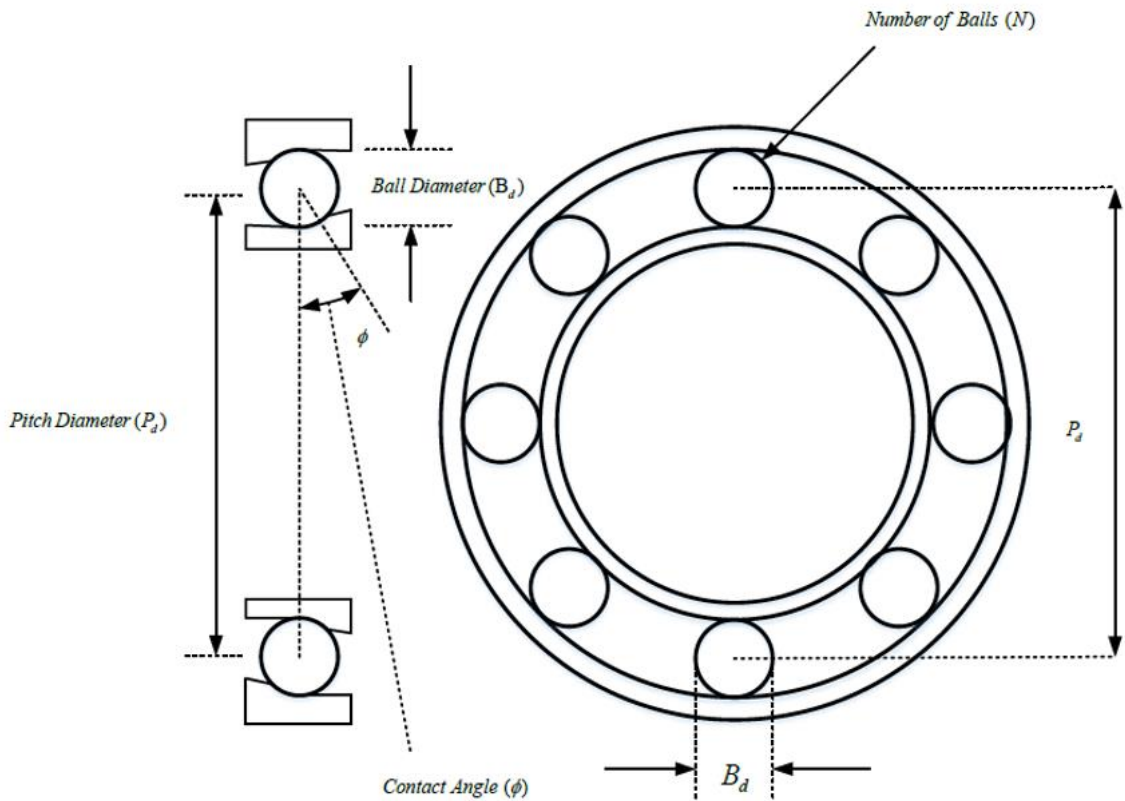


**Figure 2.6.** Bearing cross-section and its dimensions (Simatrang, 2015).

A shock pulse occurs when a minor surface crack encounters a roller ball. As the ball numbers increase, the same pulse occurs more often, which results in a higher frequency wave. The elements move at different speeds, therefore producing different frequencies.

However, as the bearing dimensions are often not known beforehand, some case studies have been carried out and the frequencies for defects can additionally be estimated using equations

$$\widehat{BPFO} = 0,4 \cdot NB \cdot S, \text{ and} \quad (8)$$

$$\widehat{BPFI} = 0,6 \cdot NB \cdot S. \quad (9)$$

If the monitoring was to be done automatically, the simplification of these equations should be considered carefully in the case of false alarms (Lindh, 2003).

Rotor unbalance, misalignments, bearing overloads, external temperatures and defective bearing lubricants cause extra stress to roller element bearings further increasing the risk of failure. Moreover, high frequency shaft voltages cause electrical currents to arc through the bearings due to stray capacitances between shaft and bearing surfaces. The shaft voltages are a result of inductive or capacitive coupling with motor windings as well as common mode voltages and currents from PWM (pulse-width modulation) inverters (Chen, 1998). Variable frequency drives (VFDs) used in e.g. pumps, fans and compressor applications also induce shaft voltages due to high IGBT (insulated-gate bipolar transistor) switching speeds while producing added harmonic frequencies. This phenomenon erodes the bearing cage's train and causes micro-craters which add up in major damage as seen in figure 2.7. The currents also deteriorate sleeve bearing's lubricants resulting in increased friction and eventually in machine failure.

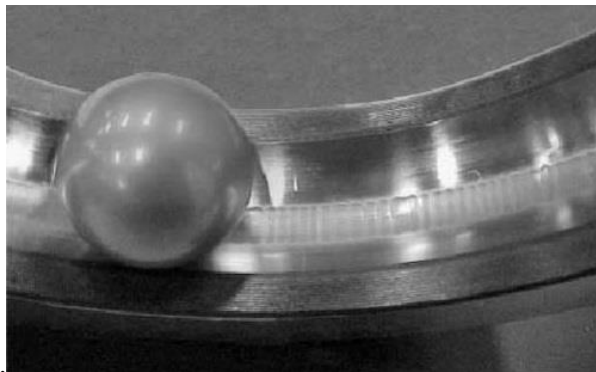


**Figure 2.7.** Damaged bearing races due to bearing current exposure (LUT, 2016).

The faults are detectable by using traditional accelerometers and speed sensors as the vibrations conduct effortlessly on the motor shaft as well as bearing cage via physical metal connections. The signals are generally picked up by transducers installed on the bearing housing.

#### **2.2.4 Sleeve bearing faults**

Sleeve bearings differ from rolling-element bearings in a sense that the supported shaft rotates on a liquid rather than mechanical rolling elements. The liquid is typically manufacturer's default bearing oil or a custom variant if necessary. The faults occur most frequently due to the degradation of this substance. Common sleeve bearing faults are oil

whirl and oil whip. On normal operation, the shaft maintains its equilibrium point and rests on the oil that keeps the shaft at a safe clearance from the bearing surface.

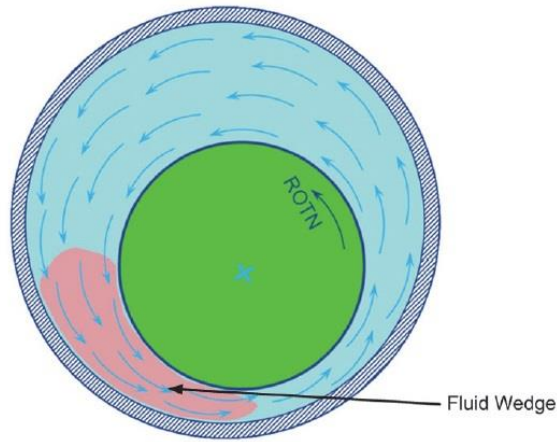


**Figure 2.8.** A shaft mounted on a sleeve bearing (API 670).

Oil whirl might occur when the bearing is insufficiently loaded, or the bearing has excessive bearing clearance. These result in radial forces on the shaft and cause excess displacement on x- and y-axes to push the system off its equilibrium. Moreover, oil whip takes place when the oil whirl frequency equals to the rotor’s natural frequency  $f_n$ . This further increases the radial energies of the shaft and causes the rotor’s center path to change. The mechanical natural frequency is calculated as

$$f_n = \frac{1}{2\pi} \sqrt{\frac{k}{m}}, \quad (10)$$

where  $k$  is the shaft’s stiffness and  $m$  is mass. The natural frequencies add together and cause devastating vibrations when the rotor speed changes since the fluid’s frequency stays at the natural value. Typically, oil whip occurs when the natural frequency is at 50 % of operating speed (API 670), and oil whirl’s frequency content is between (0,43–0,48)  $N$ .

### 2.3 Data Acquisition

For the analogue vibration data to be analyzed, it needs first to be acquired using any of the sensors presented above. The sensor’s sampling rate needs to be adequate to prevent signal aliasing. If the signal is sampled at an insufficient frequency, its digitally reconstructed version is aliased, e.g. higher frequencies show incorrectly at low frequencies therefore rendering the acquired data corrupted. Along with choosing the correct sampling, antialiasing filters are used for removing aliasing. Antialiasing is a standard technique in CM devices (PSK 5721). The signal’s sampling rate must be at least twice the bandwidth’s highest frequency, also called as Nyquist frequency

$$f_s > 2B, \quad (11)$$

where  $f_s$  and  $B$  stand for sampling frequency and signal bandwidth in hertz, respectively. Oversampling is frequently used to ensure the signal's coherence and if used with decimation in pre/post-processing, it increases SNR by pushing noise into attenuated frequency bands. The signal bandwidth is classified as the range until the measured signal's power is attenuated by 3 dB. As the occurring frequencies differ depending on the application's parameters, e.g. rotating speed and bearing dimensions, the sensors need to be carefully selected so that critical frequencies are not lost. IS/ISO 13373 recommends linear frequency ranges to be 0,2 times the lowest and 3,5 times the highest excitation frequencies in the system, while the maximum being typically 10 kHz for general frequencies. Since the amplitudes of displacement are low at higher frequencies, using a too high sampling rate results in the obtained data to be "crowded" in the left corner of frequency spectra (API 670) which results in difficulties in detecting shaft related problems. The same standard recommends good maximum frequencies to be detected as from 5 to 10 times the shaft speed. For example, for a 3000-rpm machine, the respective frequencies would therefore be from 250 to 500 Hz. According to (PSK 5721), the sampling rate shall be at least 2,56 times the upper cut-off frequency of the measuring range, e.g. sampling of 3000 Hz requires  $f_s$  to be 7680 Hz.

## 2.4 Signal analysis

Data processing analyzing techniques for vibration monitoring are several. This chapter presents only a fraction of methods while focusing on the most common techniques.

Correlation analysis: The vibration data is compared with a correlation function which gives a measurement of similarity between the measurement signal and the correlation function. Auto-correlation function attempts to find similarities in the time-delayed data version of itself whereas cross-correlation attempts the same of two inherently different signals. Auto-correlation is used as a tool for identifying repeating features in noisy signal. Cross-correlation can be used for recovering amplitude and phase of a signal that is lost in noise. The resulting graphs are called correlograms.

Spectral analysis is used to plot fundamental frequencies from a sampled wave in a frequency domain spectrum, as this wave is a sum of all frequencies and harmonics in time domain. A spectrum consists of  $L$  number of spectral lines. Increasing the amount of lines improves the resolution at the cost of measuring time. According to (PSK 5721), the relation between measuring time  $T$ , upper cut-off frequency  $f_{max}$  and the number of lines follows the equation

$$T = \frac{L}{f_{max}} = \frac{N}{f_s} \quad (12)$$

Discrete Fourier transform (DFT) is generally used to calculate spectra, for which fast Fourier transform (FFT) is generally favored method in practice due to its obvious efficiency benefits. "Cooley-Tukey" is one of the most common FFT algorithms. Further reading on

DFT and FFT are available on (Tavner, 2008). The sampling period must be carefully selected as each newly acquired data set border frequencies might be discontinuous, and this effect results in inaccurate harmonic content in the frequency spectra. The discontinuities are reduced with proper windowing.

Windowing functions are used to attenuate the border discontinuities. Windowing results in small errors on spectral amplitudes but tolerable enough to be acceptable. Popular windowing functions are Hanning, Hamming, Bartlett, and Blackman windows. Windowing functions effect on the frequency bandwidth by a certain factor, e.g. 1,5 for Hanning window, which must be considered when selecting frequency resolution (PSK 5721). Example figures of windowing effect are shown below.

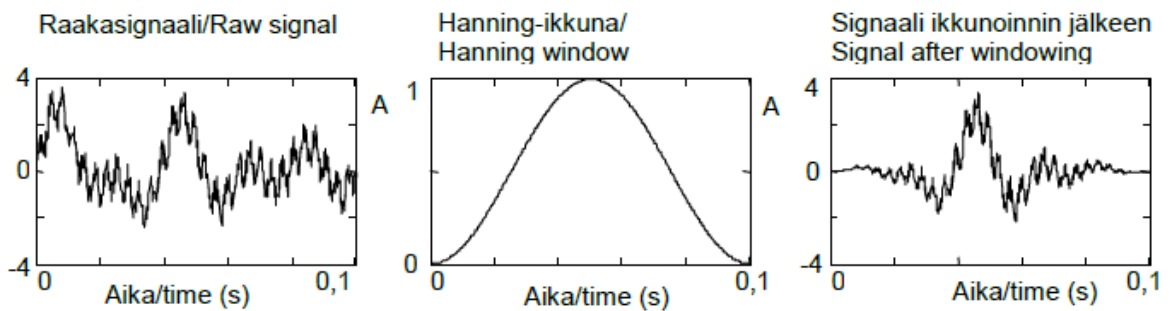


**Figure 2.9.** Hanning window effect on raw data. The windowing effectively smoothens the border discontinuities (PSK 5721).

Signal time averaging over longer timespan and trend analysis uses larger amounts of data stored on memory on a separate data file. The period is often chosen to be equal with the rotating period of the element under inspection. This method helps reducing noise from other system parts and increases the sensitivity to faults occurring on the object under investigation. However, the normal signal averaging algorithm requires impractical amounts of storage space, especially if the samples per period is e.g. 1000. This would require at least  $n$  amounts of memory for each sample which is averaged every time after a new sample is acquired. Therefore, a better, enhanced averaging algorithm that requires only two variables at a time is generally a favorable choice and easier on a calculation processor as

$$\bar{x}_n = \bar{x}_{n-1} + \frac{x_n - \bar{x}_{n-1}}{n}, \quad (13)$$

where  $n$  is the record number,  $x_n$  is the value of the corresponding  $n^{\text{th}}$  sample, and  $\bar{x}_n$  and  $\bar{x}_{n-1}$  are the average and previous average values for samples up to the amounts of  $n$ , respectively. Signal averaging should not be used on rapidly changing signal properties but rather on their signature values, such as RMS (root mean square) value calculations (Tavner, 2008). Trending can be used to estimate future fault occurrences and development by using interpolation fits on the data. Averaging can also be carried out on spectrums by calculating the averages of typically 4-8 separate spectra.

Enveloping splits the acquired signal into its upper and lower amplitude frequency components. These envelope signals are a function of the signal's peak values. The method is similar to demodulation, but the amplitude offsets are not lost.

Peak value detection can be achieved by comparing a newly acquired sample with a previous record on each iteration and replacing the previous record with the new one if the latter's value is greater than the one of the previous. The amount of storage requirement is negligible, but the achieved information can be used to set a flag for if a fault detection threshold limit has been crossed. The method is extremely prone to false alarms due to interference, so proper data filtering should be used.

Cepstrum analysis is the inverse Fourier transform of a logarithmic power spectrum whereas the normal spectrum is a Fourier transform of a power spectrum. Cepstrum analysis is used widely in applications that contain large amounts of side bands in their frequency spectra. A spectral analysis struggles at identifying these sidebands while Cepstrum analysis is better suited for it. Cepstrum analysis is a good solution in applications containing large harmonic content, such as inverter-fed induction motors (Tavner, 1987).

Overall vibration level uses a peak velocity value and compares the currently sampled peak-to-peak displacement together with rotating speed. A quantitative indicator value  $F$  is calculated according to

$$F = \frac{0.52NX}{V_a}, \quad (14)$$

where  $N$  is the rotating speed,  $X$  is the peak-to-peak displacement value in  $\mu\text{m}$  and  $V_a$  is the peak velocity value in  $\text{mm/s}$ . The overall vibrational level monitoring is popular due to large amount of available data in modern industry. This monitoring is used to set general guidelines and standards for overall machinery health analysis. According to the *Neale report* (Tavner, 2008), oil whirl, unbalance, eccentricity and misalignment can be diagnosed using the trend value of  $F$  whether it is decreasing, steady or increasing.

Shock pulse method analyses ultrasonic frequency content of 32 kHz that is a result from bearing balls passing over faulty bearing surface microcraters. The value used in this method is called a "*Shock Pulse Value*"

$$SPV = \frac{R}{n^2 F_b^2}, \quad (15)$$

where  $R$  is a meter reading value,  $n$  is the rotating speed and  $F_b$  is bearing geometry factor number. The  $R$  value relates to the severity of shock from bearings and is recorded by a well-tuned transducer, preferably dimensioned to the same resonating frequencies. Commonly a piezoelectric transducer is used for producing the meter reading. The higher the SPV, the more likely there exists bearing damage. It is commonly used along with the overall vibration monitoring according to the table 2 below.

**Table 2.** Shock Pulse Value interpretation (Tavner, 1987).

Overall Vibration Level Trend	Shock Pulse Value Trend	Comments
Low and rising	Remains low	No bearing damage.
Low and rising	Low but rising at the same rate as overall level	Bearing damage likely.
Low and rising	High value but remaining constant	Damaged bearing but other problem causing rise in level.

Plotting of shaft orbit produces information about the condition of shaft line. It is also a common method to investigate the behavior of fluid film bearings. Perfectly circular shape indicates a perfect condition as the shaft completely rotates around its central point. Eccentricity pushes the circular shape into elliptical forms, for example in the case of UMP. Unbalance and other factors may lead the orbit to differ a lot from circular shapes. Achieving a shaft orbit plot requires the use of at least two separate single-axis sensors placed at 90 ° angle so that the acquired data are plotted against each other producing an XY graph.

### 3 LUT CAPACITIVE DISPLACEMENT SENSOR

Lappeenranta University of Technology, in collaboration with ABB Finland has developed a capacitive sensor as a primary motivation for accurate control of active magnetic bearing (AMB) rotors. The commercially available eddy current sensors', such as Bently Nevada™ 3300 XL's, major flaws are their sensitivity to rotor shaft surface's roughness, non-concentricity and inhomogeneities, which result in reduced resolution and disturbances with the rotational frequency or its harmonics (Jastrzebski et. al, 2014). The capacitive sensor disregards the impact of roughness by using four different capacitive plates, which results in an averaging effect. The capacitive displacement sensor's operating principle is based on equation

$$C = \frac{\varepsilon A}{d}, \quad (16)$$

where  $C$  is capacitance,  $\varepsilon$  is permittivity,  $A$  is the area between a plate and metal surface (shaft surface) and  $d$  is the distance between the surfaces. The capacitance is inversely proportional to the distance which effects on the impedance of the resonance circuit and furthermore specifies the channel's voltage amplitude that is measured in later stages. The sensor has formerly been tested in practice in LUT laboratory in sensing and controlling the displacement of AMB motor's shaft displacement.

#### 3.1 OVERVIEW

The capacitive sensor's operation is based on measuring the resonance circuit's RMS voltage. It consists of four different capacitive plates and each of them is paired with a plate connected to ground, as seen in figures 4 and 5, resulting in eight different metallic plates in total. The sensor is capable of measuring displacement of radial x- and y-axes in a resolution of 0,16  $\mu\text{m}$ . The measurement range is in -1...1 mm in each axis.

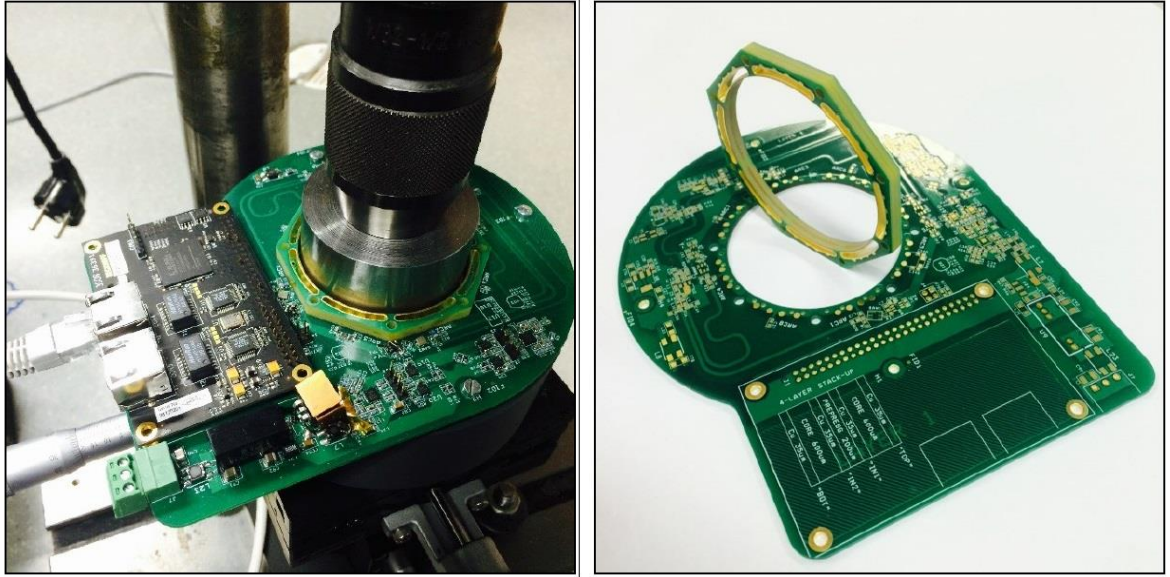


**Figure 3.1.** The latest prototype implementation of three-axis capacitive displacement sensor.

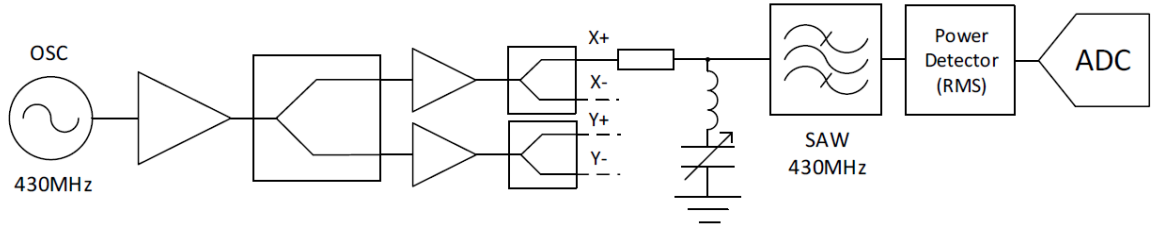


**Figure 5.** A flow chart of one of the sensor's radial position measurement signal's path.

The sensor's resonance frequency is dimensioned to 430 MHz using equation

$$2\pi f_{res} = \frac{1}{\sqrt{LC}}, \quad (17)$$

where  $f_{res}$  is the resonance frequency and  $L$  resonance inductance. The sensor has been 3D FEM modeled and the capacitance values have been approximated between  $-500$  to  $500 \mu\text{m}$  from center point, where  $-500 \mu\text{m}$  refers to  $10 \mu\text{m}$  distance between the shaft and capacitive plate. The capacitances at points  $-500 \mu\text{m}$ ,  $0 \mu\text{m}$  and  $500 \mu\text{m}$  are  $3.56 \text{ pF}$ ,  $4.45 \text{ pF}$  and  $9.37 \text{ pF}$ , respectively (Jastrzebski et. al., 2014). The 430 MHz frequency is achieved by using an inductor with an inductance of  $33 \text{ nH}$ . Changing the inductor effects on the measurement range of the sensor. The capacitance is dependent on the distance between the plates and the shaft. A SAW filter with center frequency of  $433,92 \text{ MHz}$  has been used as a band-pass filter for the later stages of sampling the resonance circuit's voltage signal. A radio frequency (RF) power detector is used to detect this resonance circuit's RMS with a conversion gain of  $7,1 \text{ V/V}_{\text{RMS}}$  at input frequency of  $450 \text{ MHz}$ , and it outputs linear-responding DC voltage. The delta-sigma A/D converter's typical sampling rate is  $10 \text{ MHz}$ . The 1-bit output from the ADC is processed by a decimating digital filter on the on-board microcontroller.

Each channel's data acquisition is integrated on the sensor's printed circuit board (PCB) and is done by feeding 1-bit data stream from delta-sigma A/D converter to a Beckhoff FB1130

piggyback controller board. The board contains a Xilinx Spartan-3E XC3S1200E field-programmable gate array (FPGA) (figure 3.2). The FPGA converts the incoming data stream into 16-bit words using a digital filter. The data is sent forwards to a separate computer via EtherCAT fieldbus for data processing and visual inspection. A standard RJ45 Ethernet interface can be used along with a CAT5 cable for EtherCAT connection. Previously, the FPGA’s purpose has been to act as a digital filter and EtherCAT controller slave bridge for further connectivity to external programmable logic controllers (PLCs) as a part of a position control feedback loop. In condition monitoring applications, the FPGA could be further developed to contain independent fault detection functionalities, which is later investigated further.

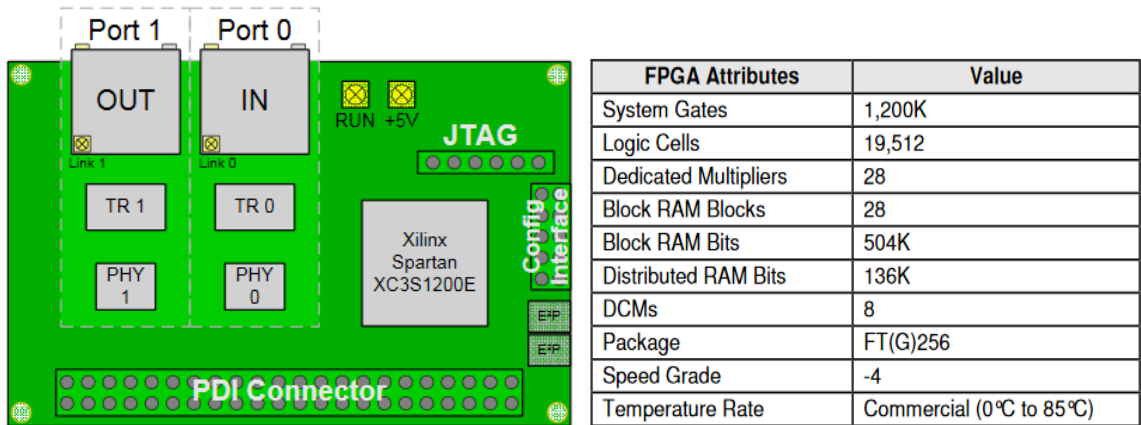


**Figure 3.2.** Beckhoff FB1130’s overview and its FPGA’s performance specifications (Beckhoff).

The FPGA is programmable using the standardized JTAG 5-pin on-board connection. The FPGA’s instructions are fetched from EEPROM on every power-up. The EEPROM configuration is done separately using the 10-pin interface. The PDI connector contains 47 pins configurable for user applications, which allows the future expansions of additional sensors. 37 pins are available for other functionalities after the displacement sensor pins.

The available on-board memory is 14,5 Mbits that could be used in data logging. Also, if off-line logging was required, a separate data storage, such as an SD-card module, should be implemented for easy analysis on external computers as an SD-card is considerably effortless to plug in and out of the sensor and the implementation of SD-card support on the FPGA is easy using the readily available functions. The FPGA can be programmed using Xilinx’s Vivado high-level synthesis programming environment, which enables the use of C, C++ and SystemC languages by converting them to hardware description language (HDL). Xilinx states that these programming languages compile bit-perfectly on to the FPGA.

### 3.1.1 Technical specifications

The sensor’s technical specifications while using a Sinc<sup>3</sup>-filter are as listed:

- Measurement target: Conductive, 58,5 mm
- Resonance frequency: 430 MHz
- Measurement range:  $\pm 1$  mm
- Nominal airgap: 1,1 mm
- ADC resolution: 0,16  $\mu\text{m}$
- Effective number of bits: 14 bits (theoretical)
- Signal-to-noise ratio: 1250 (500/0,4)
- Digital resolution: 24 bits (EtherCAT process data value)
- Sampling rate: 20 kHz
- Bandwidth
  - ADC + 256 decimation ratio digital filter: 10 kHz
  - Buffer amplifier: 80 kHz
  - RF Power detector: 17 kHz
- Noise after A/D conversion + filtering
  - Maximum:  $\pm 0,4$   $\mu\text{m}$
  - Minimum:  $\pm 0,25$   $\mu\text{m}$
- Linearity (deviation from best fit line)
  - $\pm 500$   $\mu\text{m}$  range
    - X-axis:  $\pm 2,4$  % /  $\pm 23$   $\mu\text{m}$
    - Y-axis:  $\pm 1,1$  % /  $\pm 11$   $\mu\text{m}$
  - $\pm 1000$   $\mu\text{m}$  range
    - X-axis:  $\pm 5,5$  % /  $\pm 109$   $\mu\text{m}$
    - Y-axis:  $\pm 1,8$  % /  $\pm 35$   $\mu\text{m}$
- Signal output: Digital EtherCAT fieldbus
- Power supply: 24 V, 250 mA

The 10-kHz bandwidth is enough for CM applications as the sensor measures shaft displacement and the maximum amplitudes decrease as the frequencies rise, as shown in figure 2.3. In the following sections, the desired bandwidth and digital filtering will be inspected and redesigned for better suitability in lower frequency requirements.

### 3.2 CORRESPONDENCE TO MEASUREMENT STANDARDS

API 670 standard contains requirements for machinery protection system accuracies. The requirements are listed in the table below along with the capacitive sensor's reported values.

**Table 3.** Accuracy and temperature range requirements set by API 670 and corresponding LUT sensor values.

Target	Type	Requirement	LUT sensor
Proximity probe	Deviation from straight line (slope of 7,87 mV/ $\mu\text{m}$ )	Within $\pm 25,4 \mu\text{m}$ in a range of $\pm 1 \text{ mm}$	X-axis $\pm 109 \mu\text{m}$ Y-axis $\pm 35 \mu\text{m}$
	Operating temperature range	$-35^\circ\text{C}$ to $120^\circ\text{C}$	$-40^\circ\text{C}$ to $85^\circ\text{C}$
Temperature sensor	Operating temperature range	$-35^\circ\text{C}$ to $175^\circ\text{C}$ , $\pm 2^\circ\text{C}$ over measurement range	-
Speed sensor	Accuracy	1 % of alarm level	-

The table shows that the sensor's temperature range does not comply with the standardized requirements. These limiting components are

- 680 nH inductor 0603AF-681XJRU ( $-40 \dots 85^\circ\text{C}$ )
- 27 nH inductor ELJQE27NGFA ( $-20 \dots 85^\circ\text{C}$ )
- Common mode filter ACM4520 ( $-40 \dots 85^\circ\text{C}$ )
- DC/DC converter ITTX2409SA ( $-40 \dots 90^\circ\text{C}$ )
- I/O amplifier AD8031 ( $-45 \dots 85^\circ\text{C}$ )

Additionally, the on-board FPGA's storage temperature range is  $-65^\circ\text{C} \dots 105^\circ\text{C}$ , and would be the next limiting component on the PCB. The other main components' (SAW filter, ADC buffer amplifier and AD converter) temperature ranges exceed the requirements by roughly five degrees Celsius at both minimum and maximum values. Other data acquisition recommendations listed in API 670 are shown in the table below.

**Table 4.** API 670 general recommendations for data acquisition for dynamic signals.

Target	Recommendation	LUT Sensor
A/D resolution	16-bit minimum	16-bit, tunable
Dynamic range	80 dB minimum	95 dB (ADC)
Magnitude accuracy	< 0,1 % of full-scale range	0,0015 %

### 3.3 MODIFICATION POSSIBILITIES

#### 3.3.1 Tuning the on-board A/D converter

The analogue RF signal is converted into 1-bit digital signals using the delta-sigma modulator. The A/D converter works in three separate modes that mainly differ from each other by having a varying oscillator clock frequency. An external clock source can be selected by using a mode 3 by changing the ADC's resistance and capacitance configuration. The modulator's internal clock  $f_{MCLK}$  is by default 20 MHz. This clock is fed to the modulator by half of its rate, meaning that  $f_{CLK} = f_{MCLK}/2$ . Oversampling ratio (OSR) is the ratio between ADC's output data rate and input rate. Adjustable OSR of 256 has been used previously. A higher OSR reduces the ADC's output data rate, but increases the SNR by pushing the noise to frequencies above the desired band (Texas Instruments, 2003b). The OSR must be considered when designing a digital filter in later stages. Decimation is used to reduce the output rate of oversampled data as seen in figure 3.3.

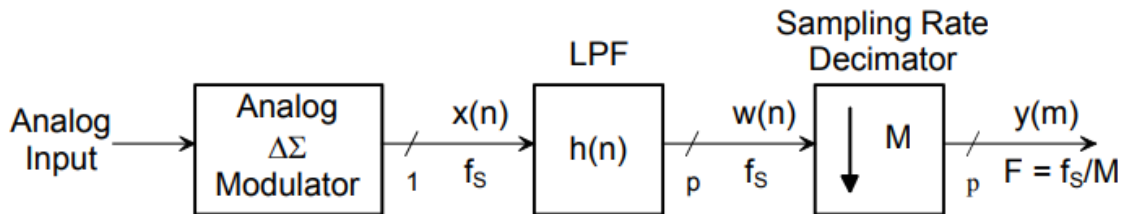


**Figure 3.3.** A basic block diagram containing a low-pass filter (LPF) and a decimator for a delta-sigma modulator.  $x(n)$  denotes the 1-bit ADC data stream,  $w(n)$  is the filtered output and  $y(m)$  is the final decimated signal (Texas Instruments, 2003).

The A/D converter's sampling rate equals the delta-sigma modulator's frequency. The modulator frequency is half of its internal oscillator frequency as in

$$f_s = f_{CLK} = \frac{f_{MCLK}}{2}. \quad (18)$$

The filtered output frequency is

$$F = \frac{f_{CLK}}{OSR}, \quad (19)$$

which leads to the default sampling ratio being roughly 39062,5 Hz (Texas Instruments, 2008a). The recommended frequency range for the external clock is 16 MHz to 24 MHz

without reduced accuracy. If accuracy loss can be tolerated, the frequencies can be extended from 1 MHz to 32 Mhz. Thus, the converter’s sampling rate’s lower and upper limits using 256 OSR would be 1953,125 Hz and 62500 Hz, respectively. The Nyquist frequencies for minimum and maximum sampling rates using equation (11) would be half of the sampling rates, resulting in minimum and maximum frequency bandwidths of 976,56 Hz and 31250 Hz. A following table summarizes the frequency characteristics. It should be noted, however, that using a lower OSR yields even higher frequency ranges at the cost of increased noise.

**Table 5.** Recommended and extended frequency ranges of the A/D converter modulator.

	Parameter	Minimum	Nominal	Maximum
Recommended values	$f_{CLK}$	8 MHz	10 MHz	12 MHz
	$B_{OSR=256}$	15,63 kHz	19,53 kHz	23,44 kHz
Reduced accuracy	$f_{CLK}$	0,5 MHz	-	16 MHz
	$B_{OSR=256}$	977 Hz	-	31,25 kHz

According to the figure 2.2, the displacement becomes less relevant at frequencies above kilohertz whereas accelerometers become more apparent. As it does not hurt to allow more band, the sensor could be tuned to support around 3 kHz to not miss any relevant information. This means, that using the prior OSR, the ADC’s  $f_{MCLK}$  should be tuned to 3,072 MHz at minimum. The master clock is tuned either dynamically by using the FPGA’s master clock or by a separate RC oscillator. However, this requires feedback signal for the clock from the FPGA which requires more PCB space. A suitable solution is to use the nominal 10 MHz clock and postprocessing the resulting signal to a smaller bandwidth using a wideband filter after the Sinc<sup>3</sup> filter within the FPGA.

### 3.3.2 *Splitting the sensor apart*

Commissioning the sensor on the rotor bearing’s outer side, as seen as the blue line in the figure 3.4 below, is rather effortless, as the sensor is possible to be pushed on the shaft while the machine is stopped. However, since the bearings’ radiuses are larger than the radius of the sensor, an installation on the inner side of the bearings (seen as the red line) requires the bearings to be removed temporarily. This increases system downtime and further prolongs installation times. To avoid motor disassembly, the sensor has been proposed to be mechanically split in half after which it could be installed around the shaft in two parts using an electrical interface between the PCB plates.

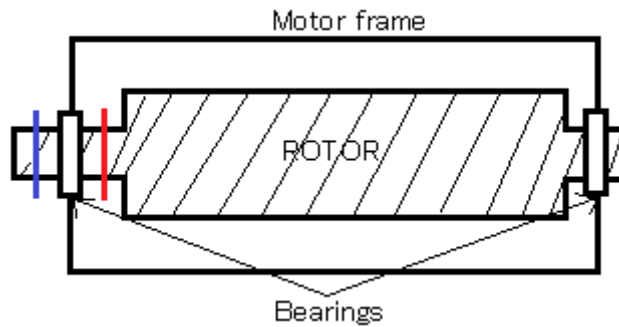


**Figure. 3.4.** Side profile of a rotor with red and blue lines representing sensor locations.

The sensor's capacitive plates are positioned precisely as the absolute distances are roughly  $100\ \mu\text{m}$  from each other. These relative distances set the limits the sensor can measure accurately. Cutting the sensor apart increases the distances between the plates chaotically and therefore their positioning accuracies deteriorate, leading into the loss of measurement accuracy and reliability. An extremely accurate support frame for the capacitive plates would be needed to keep the plates' distances constant.

Furthermore, the RF waves produced by the single 430 MHz oscillator would have to propagate through a connector interface. Therefore, the RF connector interfaces are required not to cause different signal diminishing between separate channels. This issue could be resolved by using multiple RF oscillators on each measurement channel. This solution proposes further problems, however. Channels with multiple oscillators would need to be synchronized with each other using a lower frequency clock, such as  $1/32 \cdot f_{osc}$ . Due to small individual differences between the channels, each of the channels' signal phases would be varying, which may result in coupling between the channels and this leads to additional modulation of each channel's outgoing RF signal. In summary, synchronizing the channels is challenging and proposes plenty of issues (Tolsa, 2017), but is possible by developing a new design.

### 3.3.3 *Slave controller*

The capacitive sensor's onboard FB1130 piggyback EtherCAT controller was chosen during the sensor's initial design phase. Beckhoff has since replaced the production of the FB1130 version with new FB1111 and FB1131 evaluation controller boards. However, these boards have replaced the FPGA with an ET1100 ASIC (application specific integrated circuit) with the functionality focus in EtherCAT. Since ASICs are hard-coded, these chips cannot be modified to support digital filtering unless included in the design, thus requiring an external microcontroller to preprocess data for it. To keep the previous functionality present, an alternative microcontroller capable of industrial communication needs to be searched for. The ABB AC500-CMS contains by default a terminal base TF5X1, which supports Ethernet as a communication protocol by default. EtherCAT uses the standardized IEEE 802.3 Ethernet frames, allowing the use of normal network card on the receiving end.

Aside from EtherCAT, other protocols are also available for industrial Ethernet. One major limiting factor is synchronicity of slaves together as this way the phase difference of the unbalance excitation is possible to be detected when planting the sensors on the different motor shaft ends. Some previous study lists ProfiNet IRT, CC-Link IE, Sercos III and EtherCAT protocols to contain synchronic operations (Ethercat, 2014). Furthermore, the option of link topology is a great feature as the master controller requires only one input link this way. The slaves are connected directly together with only one end visible to the master in the link topology. The link topology also allows spreading slaves over wider areas if the distances between the slaves will not grow too large. For example, if a factory contains several machines located over wider areas, all of them are connectable to one PLC this way by “serializing” the slaves together. All the four protocols listed support line structure, but some with certain noticeable limitations. ProfiNet suffers from performance loss depending on the topology. The link slave limits of ProfiNet IRT (10) and CC-Link IE Field (121) are significantly less than the two counterparts: 511 using Sercos III and 65535 on EtherCAT. Additionally, EtherCAT suffers from practically zero performance drops as the number of nodes increases. EtherCAT and Sercos III are the most cost-efficient solutions from the four. Moreover, the ProfiNet and EtherCAT are directly compatible with AC500-CMS. Some research did not find compatibility of Sercos III and CC-Link with AC500 communication modules. The table below summarizes the differences between these four protocols.

**Table 6.** Summary of industrial Ethernet protocol comparison (Ethercat, 2014).

	ProfiNet IRT	CC-Link IE Field	Sercos III	EtherCAT
Synchronicity	Yes	Yes	Yes	Yes
Supported topologies	Line, tree, star	Line, star	Line, ring	Line, tree, star, ring
Line structure N.o. nodes	10	121	511	65535
Node interface costs	OK	N/A	Good with FPGA	Extremely good with FPGA/ASIC
Special hardware	Special chip on master and slave	Special chip on master and slave	Special chip on master and slave	Special chip on slave, no special chip on master
Technology stability	N/A	N/A	N/A	Good
AC500-CMS support	Yes (CM579)	N/A	?	Yes (CM579)

A key feature of EtherCAT is its ability to be implemented on any master computer that is equipped with an ethernet port. This allows connecting the sensor to practically every computer and is therefore not limited to only industrial computers. The other features also keenly favor EtherCAT, especially when considering the costs and device limitation

numbers. Furthermore, EtherCAT specific distributed clock is used to synchronize the slave controllers easily. AC500 CM579 EtherCAT master also supports the distributed clock.

FPGAs can provide true parallelism in its execution procedure whereas traditional microprocessors achieve virtual parallelism by context switching and threading. The LUT sensor currently contains four digital 1-bit input channels that are digitally filtered at the same rate as the ADC's modulator sampling rate. Therefore, the logic controller must meet certain speed criteria, especially when four channels are digitally filtered in parallel. A standard microprocessor needs to do extra read and write instructions along with summations and multiplications while filtering, which makes designing by clock cycles not straightforward. In e.g. four channel digital filtering application, a microprocessor needs to execute at least four times the same clock cycles when compared to a parallel processing FPGA. For example, assigning a logic gate output into a certain variable requires only one clock cycle from an FPGA whereas a microprocessor needs to fetch variables from memory and execute several instructions over higher number of cycles to achieve the same result.

Alternative solutions, such as a CPU added with a coprocessor are available, for example TI C2000 Delfino microcontrollers (Texas Instruments, 2017c). TMS320F2837xD and TMS320F2837xS models contain a separate, programmable control law accelerator (CLA) that works independently of the main CPU, increasing throughput. These microcontrollers are identical except for that the other model contains a dual-core CPU. The chips also contain four separate 16/12-bit ADCs that produce 1,1/3,5 MSPS output rate and eight sigma-delta converters. These 16-bit ADCs can be used to remove the need of the ADS1203s, effectively reducing PCB size and costs. Furthermore, the temperature ranges comply with the -40 to 125° C standard. The ADCs' SNRs using 16-bit differential mode is 87,6 dB. However, EtherCAT communication requires an external EtherCAT module. TI uses the ET1100 in one of their example EtherCAT solutions, as seen in (Texas Instruments, 2017d). Even though CANopen is possible to be used on these chips as they support CAN output by default, it requires knowhow of programming the CANopen protocol layer. The pricing of these microprocessors starts from \$ 11,32 and \$ 14,33.

For FPGAs, Beckhoff's EtherCAT IP Core is required for EtherCAT communication. The IP core supports a high number of FPGAs since it does not instantiate dedicated FPGA resources (Beckhoff, 2015). Beckhoff lists certain Xilinx and Altera FPGAs to be suitable with EtherCAT IP core. Altera FPGA EtherCAT software also supports other industrial communication protocols with the same application peripheral interface, such as PROFINET, POWERLINK and Modbus TCP (Softing, 2017). The requirements for minimum amount of logic elements (LE) for FPGAs for the EtherCAT IP core can be set in accordance with (Ethercat, 2017a), (Ethercat, 2017b) However, the amount of LEs in practice are a lot higher as the chip contains functionalities along with the EtherCAT.

**Table 7.** EtherCAT compatible chips with operating temperature range of -40...125 °C.

	Manufacturer	Supported FPGA families
FPGA	Altera / Intel	Cyclone: III, III LS, IV E, V, V SoC Stratix: II, IV E, IV GT, IV GX, V Arria: II GX, V, V GZ Intel Atom E6x5C Max 10
	Xilinx	Spartan: 3, 6 Kintex: 7 Virtex: II, X, 4, 5, 6, 7 Artix 7 Zync
	Infineon	ARM Cortex -M4 series

In summary, traditional processors must be joined with an ASIC for EtherCAT functionality whereas all FPGAs listed in the above table are available with its direct support. The table shows some suitable alternatives to FPGAs but most of the microprocessors' ADC resolutions are 12-bit at best. The market contains a lot of alternative devices in the industrial temperature range (up to 85 °C).

### 3.3.4 Additional sensors

For using external sensors on the PCB, a multiplexer controlled by a microcontroller between the data acquisition and these sensors is implementable. This way a single A/D converter digitizing multiple channels could be used, which saves on-board space and costs. However, the nonlinearity produced by multiplexer switching must be considered especially in channels that operate at higher frequencies.

#### 3.3.4.1 Temperature sensor

To measure bearing temperatures, a CMOS temperature sensor might well be attached to the bearing frame. Commercial temperature sensors are available with analogue and digital outputs. The standardized temperature sensors are 100-ohm, platinum, three-lead RTDs or thermocouples (API 670). If an analogue output sensor is used, additional PCB area is required for an interface circuitry. The circuitry generally consists of a voltage amplifier and an ADC. In theory, one analogue temperature sensor could be attached to one displacement measurement channel and triggered using a multiplexer that could be controlled via FPGA. However, using a multiplexer hinders the displacement measurement and will also cause nonlinearities due to switching which easily leads to false alarms. Another solution is to use a separate channel with one multiplexer and an additional ADC for slower rate measurements, including temperature and speed measurements. Yet another solution is using a  $\mu$ C that contains several built-in A/D converters. Additionally, temperature sensors with a

digital output could be connected directly into the  $\mu\text{C}$  digital input pins, which requires no complex connections to existing ADCs.

A digital output temperature sensor, TI LMT01-Q1 (Texas Instruments, 2017) can measure temperatures in a range of  $-40^\circ\text{C}$  to  $150^\circ\text{C}$  with a resolution of  $\pm 0,0625^\circ\text{C}$ . Absolute temperature ratings are stated to be from  $-65$  to  $175^\circ\text{C}$ . Table 3 shows the standardized required values for a temperature sensor in CM. The LMT01-Q1's maximum operating temperature falls short by  $25^\circ\text{C}$ , but since the LUT sensor must be within 75 mm to the bearing surface, these extreme temperatures can damage the PCB itself as well. Another digital temperature sensor met the standardized criteria which also contains a digital output, such as (Analog Devices, Inc., 2012). However, a price query at Mouser webpage shows that its price tag is \$ 90,90 whereas the LMT01-Q1 costs roughly 2 €.

The sensor's output is designed so that the software implementation on a microcontroller can be done effortlessly. Its target applications feature automotive, HVAC (Heating, Ventilation, & Air Conditioning) and power supplies. A wire with a maximum length of two meters can be used with the sensor. When mounting the sensor, it must be electrically insulated from the bearings in case of circulating currents to meet API standards.

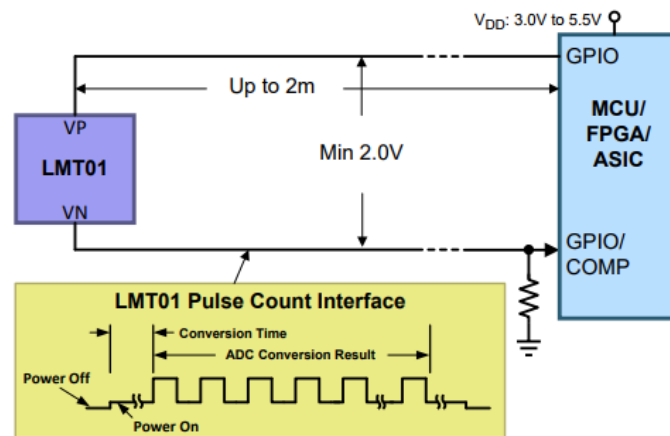


**Figure 3.5.** LMT01-Q1 connectivity to a logic controller (Texas Instruments, 2017).

This type of sensor can be mounted on a bearing surface using adhesive. The vibrational forces must be considered when creating a mounting solution so that the temperature sensor does not become damaged. Of the two sensors presented above, neither was provided with vibrational force endurance values, however. Some analog platinum RTDs, such as (Heraeus, 2016), are supplied with vibrational resistance values. Implementing an ADC driver using oversampling would not be complicated as the temperature change has large time constants and low amounts of noise. Frequency range for temperatures measurements are roughly 10 Hz (National Instruments, 2016). The acquired data from the sensor could be used without filtering, but noise rejection of input supply voltage frequency 50 Hz is suggested along with RTD excitation and thermocouple's cold-junction compensation. The wiring for RTDs to monitoring systems should be a three-conductor shielded wire in accordance with API 670.

#### 3.3.4.2 *Speed sensor*

The shaft rotational speed could be estimated using the capacitive plates. By knowing the signal period, the rotational speed is calculable. With a sufficient stimulus, as a certain discontinuity on the surface, the period is easy to estimate directly via monitoring a distinguishable spike in data. However, API 670 states that the surface areas observed by the proximity probes must not contain mechanical discontinuities, such as keyways or oil holes. Thus, if a standard compliant sensor was desired that uses a keyway in its implementation, an external speed sensor would be required. Nonetheless, as the practical measurement results show in the future chapter 4, the speed is possible to be estimated. Some proposed algorithms for speed estimation include zero crossing detection, implementation of phase-locked-loop with a sine signal and local peak interval detection.

#### 3.3.4.3 *Acoustic sensor*

As the FPGA's maximum internal clock speed is 572 MHz, it can potentially sample signals up to 236 MHz without signal losses. Bandwidths of AE range typically from 100 kHz up to 1 MHz. A similar ADS1203 ADC is sufficient up to signal rates of 16 MHz. A band pass filter with lower and upper cutoff frequencies of 100 kHz and 1 MHz sampling at greater than 2 MHz rate is achievable on the FPGA. For filters used in  $\Delta\Sigma$ -ADC decimation, the Sinc<sup>3</sup> filter could potentially act as a 1 MHz low-pass filter which would be fed into a 100 kHz high pass FIR filter.

### 3.3.5 *Additional output links*

Different ways to transport data from the sensor is useful in industry as the current EtherCAT connection might not be found on the most PLCs. Implementation of, for example, analogue connection would make the sensor compliant with virtually any device that contains an A/D converter. An analogue connection also lessens the requirements on the capacitive sensor by removing the need of the onboard digital circuits and ADCs.

A proposed wireless connectivity has a possibility of installing the sensor on any places difficult for humans to reach and maintain. There is also interest in developing the sensor completely wireless and therefore being virtually fully wireless, as the sensor can be powered from a local battery. Some future work could also contain powering the sensor via motor magnetic excitation.

#### 3.3.5.1 *Analogue connection*

An analogue 4...20 mA output has been proposed to be included in the sensor. A coaxial cable or a twisted pair can be used for data transfer, but the voltage output of the ADC buffer amplifier needs first to be scaled to represent 4...20 mA range using a series resistor. As the AC500's analogue sampling rate is 50 kHz, the maximum sensor's analogue output bandwidth according to Nyquist's rate would be 25 kHz. To ensure the desired bandwidth to stay consistent, a Texas Instruments 4...20 mA current loop transmitter XTR115 (Texas Instruments, 2003) can be used, for example.

However, as the sensor contains an individual channel for each measurement axis, the analogue connection would be impractical due to size requirements. Each channel would require a separate analogue cable. The current control loop that is required for the analogue connection also needs to be powered up from either the sensor or the receiving end. As the industrial computers often contain an analogue connection inputs, they are also equipped with a current control loop beforehand, meaning that the power supply for the current loop would be more practical to be taken from the receiving end. This also saves space from the PCB as the current loop requires an external transistor to drive power to it.

The ABB FM502 function module supports analogue connections up to 100 meters at maximum for each channel using a shielded cable (ABB, 2017). API 670 recommends communication wires to be of type 16 AWG (American Wire Gauge) to 22 AWG with 1,9 mm thick insulation. As the analogue signal from the RF power detector is 0,1–5 V DC, the cable thickness is not a factor in the cable skin effect and thus the least resistivity cable shall be used. The resistivity of 16 AWG is 13,17  $\Omega$ /km and the analogue input resistance of FM502 is 27  $\Omega$ . The maximum cable length is limited by the voltage drop due to the loop resistance that consists of the two-way cable resistance and input resistance. The XTR115 can operate in voltage range of 7,5–36 V while the FM502's input range is selectable

between +2–18 V (IEPE) and -10–10 V. The voltage drop can be calculated using Ohm's law

$$U = RI. \quad (20)$$

The voltage drop of the current loop of 20 mA signal is

$$\left(27 \Omega + 2l \cdot \frac{0,01317\Omega}{m}\right) \cdot 0,02A. \quad (21)$$

If the loop transmitter is supplied with 24 V and the loop's voltage is 10 V, the allowable voltage drop becomes 14 V. The maximum distance that yields 14 V drop therefore equals roughly 25,5 km. At these distances the cable most likely is more susceptible to EMI and RF interferences as well as the cable costs becoming a major factor. 1 V drop results from 873 m cable, which also allows lower voltage usage of the loop's power supply.

### 3.3.5.2 Wireless connection

For applications where the sensor would be mounted inside a motor frame, a wireless communication would save cabling requirements. A wireless network module could be added on the PCB that is connected to the EtherCAT driver's PDI output connections. The board contains 16 different 16-bit output pins that can act as a data output for serial peripheral interface (SPI) for general WLAN modules as well as other chips.

A query on Mouser Electronics webpage for SPI WLAN modules results in a Lantronix PremierWave 2050 module (Lantronix, 2016) for roughly 3 € price. Maximum operating temperature is 85 °C. Its throughput, or maximum data rate, is 54 Mbps, which virtually does not limit the sensor bandwidth at all.

The data can also be sent periodically in larger packets, which does not limit the sampling speeds, but requires more on-board memory. The chip itself contains 32 MB of DDR2 DRAM which can be used as temporary data buffer.

## 3.4 FPGA LOGIC

The ADC modulator contains a certain amount of noise by default. A second-order delta-sigma modulator's quantization noise increases with frequency up to the Nyquist frequency, as seen in figure 3.6 below.

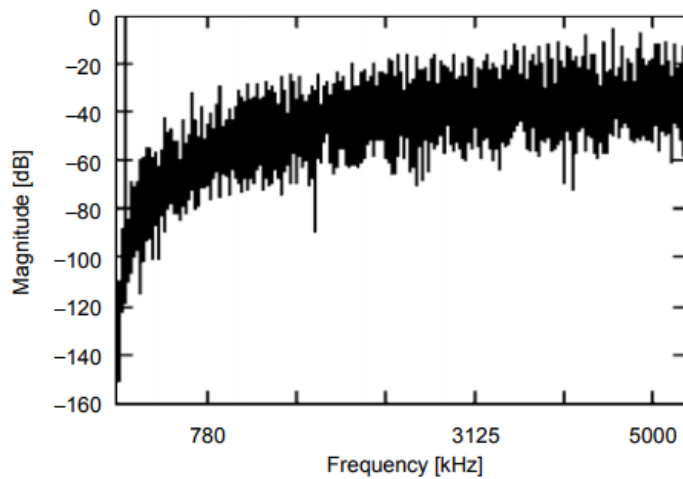


**Figure 3.6.** A second order delta-sigma modulator quantization noise (Texas Instruments, 2003b).

The signal noise can be further reduced using digital filters. Especially frequencies above the desired bands should be filtered out. If the PCB was supplied with additional sensors using different frequency bands, several kinds of digital filters can be implemented on the FPGA. The on-board memory allows the use of multiple parallel filters that could be selected using a switch in applications where a single channel carries several different variables. The data processing on the FPGA should be limited to values that do not require graphical interpretation, e.g. calculation of peak-values and time-averages.

If the sensor is supposed to be used as a real-time data-acquisition board in between the motor and a monitoring system, the digital filter used shall be linear-phased and its response time must meet the real-time criteria. Nearly every symmetrical finite impulse response (FIR) filters are linear-phased by nature (Mathworks, 2017a). Additionally, FIR-filters are generally stable and synthetization on hardware is simple. Other filter type, infinite impulse response (IIR) filter, uses feedback in its design, which might cause them to be unstable without thorough design. IIR-filters use less memory blocks than FIR-filters, but they contain nonlinear phase-delay, which makes them not desirable in real-time applications. On the other hand, postprocessing techniques can be more advanced using IIR-filters if a raw data set has been collected beforehand. Non-causal zero-phase filters can be used to eliminate nonlinear phase distortions of IIR-filters (MathWorks, 2017b).

API 670 recommends the frequency range to be fixed using a field changeable band-pass filter or a combination of low pass and high pass filters. The passband ripple shall be within 0,5 dB of the input signal, and a minimum roll-off rate must be 24 dB per octave.

### 3.4.1 Digital filtering

A Sinc filter, also known as cascaded integrator-comb (CIC) filter, is one of the most used decimation filters in delta-sigma A/D converters. The filter converts the incoming 1-bit data

stream to  $n$ -bit word. A  $\text{Sinc}^K$  filter is an attractive choice since it requires no digital multipliers in its hardware implementation. A transfer function for a  $K$ -degree Sinc filter is

$$H(z) = \left( \frac{1}{M} \cdot \frac{1-z^{-M}}{1-z^{-1}} \right)^K, \quad (22)$$

where  $M$  is the decimation ratio and  $z$  is a delay element. It is seen that the filter consists of  $K$  stages of FIR filters and therefore having constant group delay. The frequency response of a  $\text{Sinc}^3$  filter is shown in the following figure 3.7. At the cost of filter length, some noise will be present from out-of-band frequencies.

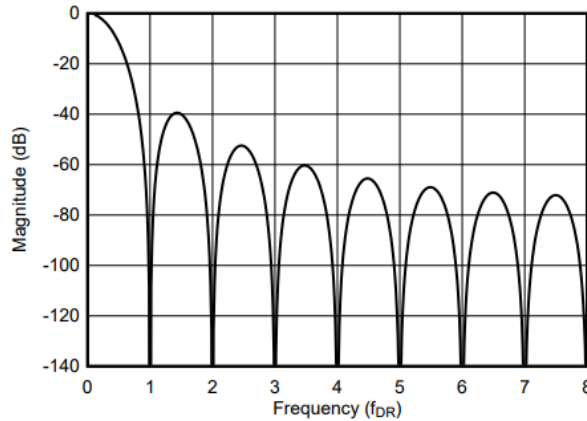


**Figure 3.7.** Frequency response of a  $\text{Sinc}^3$  filter (Texas Instruments, 2017b).

According to (Texas Instruments, 2003b), the order  $K$  of the  $\text{Sinc}^K$  filter should be at least one degree higher than the order of the modulator

$$K \geq 1 + (\text{order of } \Delta\Sigma), \quad (23)$$

which can be used to calculate the output bus width of the filter combined with a 1-bit  $\Delta\Sigma$ -modulator by

$$p = 1 + K \cdot \log_2 OSR. \quad (24)$$

The Sinc filter's bandwidth can be estimated to be 0,262 times the modulator data rate  $f_{\text{data}}$ . Using the aid of (Texas Instruments, 2003b), a similar table (8) can be used to summarize the filter, but for  $f_{\text{MCLK}}$  being 3 Mhz.

**Table 8.** A summary of Sinc<sup>3</sup> filter's output word width and bandwidth in respect with the  $\Delta\Sigma$ -modulator's  $f_{MCLK}$  being 3 MHz.  $OSR$  = decimation ratio,  $DR$  = data rate,  $f_N$  = Nyquist frequency and  $p$  = number of bits.

OSR	$DR$ [kHz]	$f_N$ [kHz]	$p$ [bits]	-3 dB point [kHz]
4	384	192	7	100,6
8	192	96	10	50,3
16	96	48	13	25,2
32	48	24	16	12,6
64	24	12	19	6,3
128	12	6	22	3,1
256	6	3	25	1,6

For vibration monitoring, a decimation ratio of 128 can be used with  $f_{MCLK}$  of 3 MHz to achieve a filter bandwidth of near 3 kHz using a Sinc<sup>3</sup> filter. The output word size of the filter should match the bit width of the modulator. The least significant bits (LSBs) can be disregarded at the filter output to match the word size.

The Sinc filter can be implemented using cascaded structure of three integrators and three differentiators. The first stage integrators' sampling rates should match the A/D modulator's sampling rate  $f_s$ . The third integrator's output is decimated down by  $M$  which is then fed to the first differentiator's input at a sampling rate of  $f_s/M$ , as seen in figure 3.8.

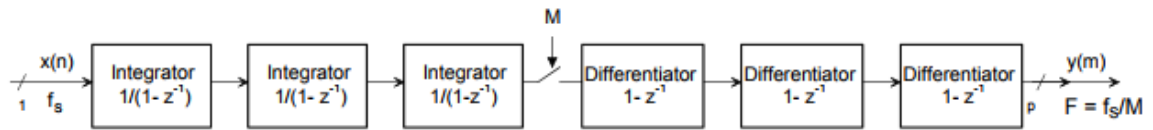


**Figure 3.8.** Block diagram of a Sinc<sup>3</sup> filter (Texas Instruments, 2003b).

ENOB (Effective Number of Bits) and SNR can also be calculated from the decimation ratio for the 2<sup>nd</sup> order  $\Delta\Sigma$ -modulator. The equation for ideal SNR is

$$SNR_{ideal} = 6,02 \cdot N + 1,76 - 20 \cdot \log \left[ \frac{\pi^K}{\sqrt{2K+1}} \right] + (20K + 10) \cdot \log(M), \quad (25)$$

where  $K$  is the order of the  $\Delta\Sigma$ -modulator and  $N$  is the ENOB. For 2<sup>nd</sup> order modulator the  $K$  is 2. The following table can be used to summarize the effect of different  $M$  values on the SNR and ENOB

**Table 9.** Decimation ratio (*OSR*) effect on SNR (Signal-to-noise ratio) and ENOB (effective number of bits) of a 2<sup>nd</sup> order  $\Delta\Sigma$ -modulator (Texas Instruments, 2003b).

OSR	SNR <sub>ideal</sub> [dB]	ENOB <sub>ideal</sub> [bits]
4	24,99	3,9
8	40,04	6,4
16	55,09	8,9
32	70,14	11,4
64	85,19	13,9
128	100,24	16,4
256	115,30	18,9

Wideband filters contain almost ideal passband properties and steep stopband transition curve as seen in figure 3.9. A half-band filter is a typical decimating wideband filter. Wideband filters are slower than a Sinc filter due to their higher order, which shows as a small delay between the input and output. This delay results in these filters being not suitable for signals that are multiplexed. However, due to superior passband ripple and hence minimal distortion of obtained values, the filters are better suited in applications that are not time-critical, as in condition monitoring.

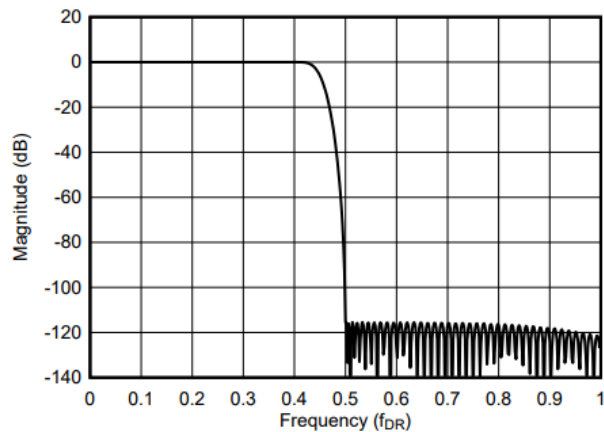


**Figure 3.9.** Frequency response of a typical wideband filter (Texas Instruments, 2017b).

Using multiplexed input sources are not preferred due to higher pulse rise times of higher order filters. If a signal source was rapidly switched, the previous signal's values would still be passing through the filter and would therefore corrupt the new values until enough clock cycles were passed through. One solution is to disregard some number of samples after a channel switch by using a delayed flag. For linear phase filters, the delay equals roughly half of the number of filter length. For example, the delay for a 50<sup>th</sup> order, 10 kHz FIR filter is 2,5 milliseconds. Another solution is to use a parallel filter connected to a separate multiplexer that is controlled by the signal that controls the signal sourcing multiplexer. When a different signal is selected, the respective filter for that signal is selected simultaneously. This implementation requires more memory on the chip, however.

### 3.4.2 Programming the chip

The filtering is coded on the FPGA using Xilinx's System Generator -tool. The program allows programming the chip using Simulink models and they are stated to be compile bit perfectly. The following picture depicts the data acquisition program implementation which is also used in modeling the code simultaneously.

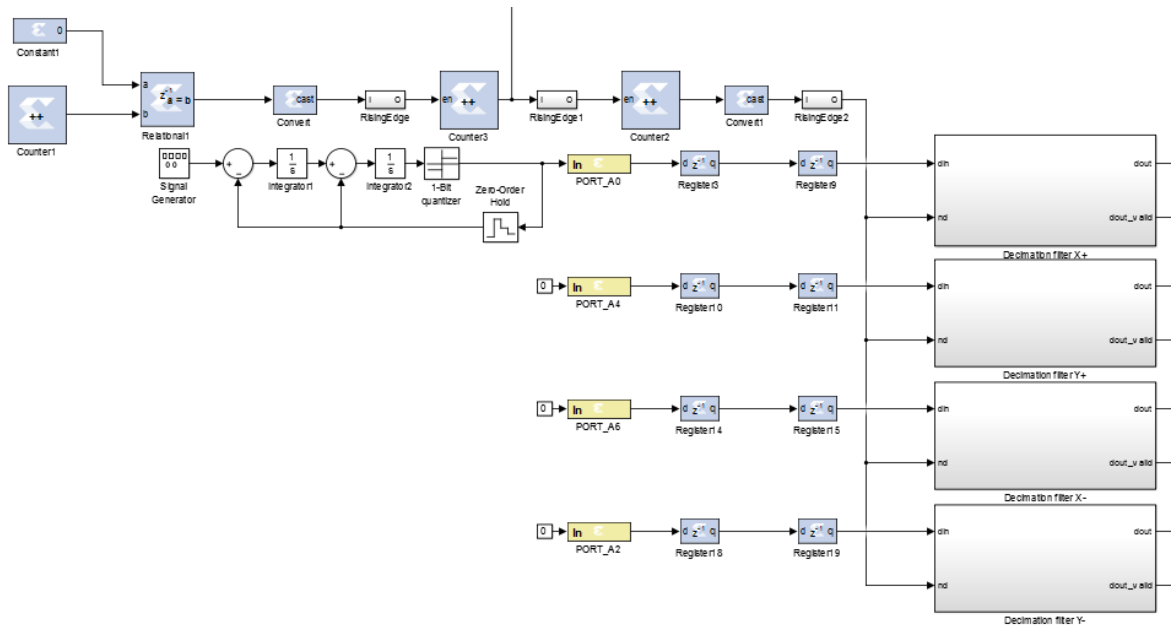


**Figure 3.10.** The first part of data acquisition program on the FPGA using Xilinx's System Generator.

The model contains a second order delta-sigma modulator as X+ channel's input. The modulator's frequency is 10 MHz. The decimation filters receive synchronized enable clock source and the ADC's signals as their sources. The decimation filters are implemented using Xilinx's premade function blocks. The CIC Compiler 2.0 works on the Spartan 3E -series. The filter samples at 10 MHz speed with a decimation ratio of 256. The output data width is scaled to 24 bits according to the equation 24. The design parameters of the CIC filters are presented in appendix I.

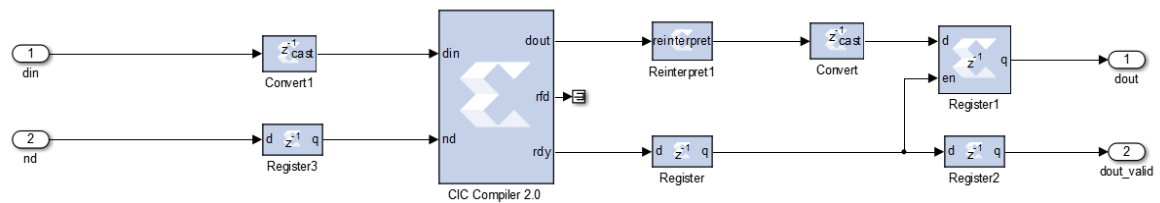


**Figure 3.11.** The implementation model of the CIC filter on the FPGA.

The outputs are afterwards fed to wideband FIR filters. The following code shows the design of the filters using Matlab.

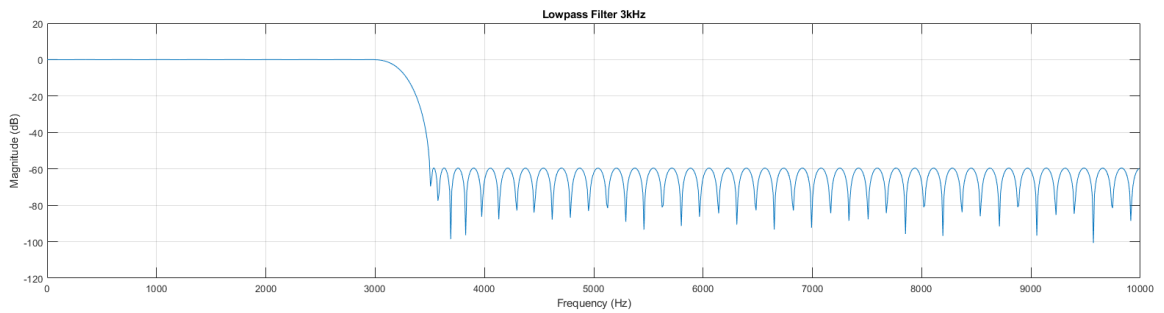


**Figure 3.12.** Frequency response of a designed 3 kHz low-pass FIR filter.

Additionally, a prototype speed estimator based on results from chapter 4 was implemented. The model works by detecting peak values and calculating the time between the pulses. To remove local peaks in between the cycle phases, a lower limit threshold from previous maximum peak is included. The program does not calculate the signal unless the value raises over the lower limit. Additionally, a low frequency filter is also recommended in the input to smoothen out the signal. Also, a moving average signal working as a limit trigger has been successfully tested in practice in real-time on TwinCAT using a Simulink model.

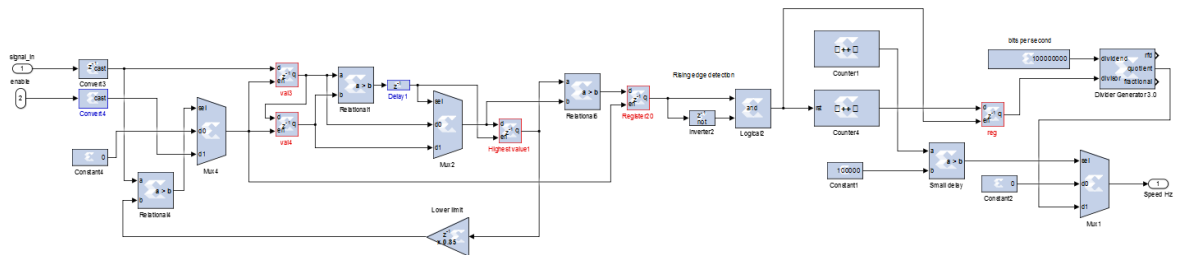


**Figure 3.13.** Prototype model of a speed estimator.

A simple peak value detection and its value hold is presented in the following figure (3.14). A user input reset signal is necessary as the model holds the signal of external disturbances and displacement peaks are large during motor startup.

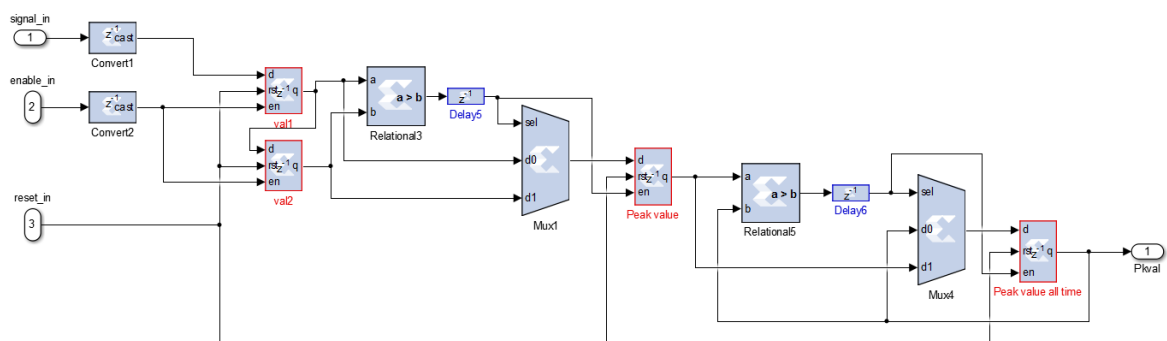


**Figure 3.14.** Model of peak value detection.

Other signals, such as separate activation and reset signals might also yield beneficial as optional user inputs.

### 3.4.3 Data storage

The vibration data is possible to be sampled and stored periodically, e.g. in three second intervals after a certain signal. API 670 recommends online DAQ systems to store data periodically on a time basis, for example once per hour, once per day, and so on. The data should be saved for 24 months. The data storing process can be started autonomously by using an onboard timer, an exception signal or a user request via fieldbus connection. The alert signal can be implemented to observe single axis amplitude, and trigger data storing function if the peak amplitude exceeds a certain limit. Storing the 16-bit data of two axes over three seconds at 3 kHz requires 288 kbits of storage space. Theoretically, the 14 Mbits of BRAM can store this data over 104 seconds. If the data is stored hourly, the amount of storage used after 24 months would be roughly 5 Gbits. Reducing the measurement period to a daily or weekly basis, the amount of space required is 2,1 Gbits and 30 Mbits, respectively. The logging time should be reduced to one second, which uses 10 Mbits of space if the data is stored weekly. In addition, the data is lost on every power-off. If additional sensors were added, even more space will be used, especially in higher frequency applications. An external memory card would be a suitable solution as it also eliminates the need of a communication link if the data collection is not necessary in real-time. The FPGA software might also use BRAM in its implementation, depending on how complex the program is. Another solution is to store the data on an external computer.

## 3.5 CALCULATION PLATFORM COMPARISON

### 3.5.1 On an industrial PC

#### Advantages

- Large signal processing and CM libraries available allowing fast application specific developing.
- Multiple industrial programming languages are supported enabling wider audience to create programs.
- Calculation can be combined with additional sensors enabling more complex algorithms.
- Real-time data comparison with external devices is possible depending on the communication protocol in use.
- Possible to gather external data from cloud for more complex algorithms.
- Modifying the post processing code is easy and often possible on the field.

#### Disadvantages

- Requires continuous communication link to sensor to acquire data.
- Communication link might limit bandwidth or requires preprocessing of data.

### 3.5.2 *On the capacitive sensor*

#### Advantages

- Less need for volumetric space as no computer is needed in vicinity.
- Lower energy consumption if the sensor is used as a monitoring system to replace the need of an external computer.
- Large signal bandwidths. The bandwidths are mainly limited by the FPGA and digital filter lengths.
- No post processing required on front-end allowing fast access to data analysis.
- The program is hidden from public making troubleshooting easier in case of malfunction. No need to question the customer of possible program modification.

#### Disadvantages

- Limited memory might limit implementable functionalities.
- The FPGA requires an experienced HDL programmer unless third-party vendors support compatible code libraries on other languages.
- Xilinx programming environments' license costs.
- Code modification requires more work.

## 3.6 COMMISSIONING ON THE MACHINE

As the sensor should be mounted around the machine shaft without it being in physical contact with any of the surface area, it is imperative to be mounted on a separate support system. As VFD driven motors tend to produce circulating currents on the frame, a proper mounting plate with good grounding is ideal to reduce noise. The metal support plate needs to be mounted on the frame in such a way that the vibration of the frame does not disrupt the measurement accuracy. The sensor shall be mounted within the motor only if the absolute values are not attainable from outside. Otherwise it should be placed in locations that allow adjustment and removability while the motor is in operation (API 670). In the case of sleeve bearings, the sensor shall be located within 75 mm of the bearing and orientation shall be so that the X and Y-axes are measured  $45^\circ \pm 5^\circ$  from the shaft's vertical center (API 670). International standard ISO10816-3 classifies support flexibilities in two categories: rigid and flexible support systems. A support system, that is a combination of the machine and the foundation, e.g. metal PCB support plate, is rigid if the natural frequency of the system is at least 25 % above the highest excitation frequency of the machine, which is generally its rotating speed. Other systems are classified as flexible. The rigidity can be dimensioned only on the measurement direction and flexible on the other. Typically, medium and large-sized machines are equipped with rigid systems, while turbo motors and -generators above 10 MW use flexible support systems (ISO10816-3). ISO7919-5 recommends that the lowest natural

frequency of the transducer support system should be at least seven times the synchronous rotational frequency while not being a multiple of it. To achieve rigidity, either plastic or rubber screws with appropriate dimensioning can be used, or otherwise a separate mounting system is possible to commission on the floor on the motor drive end. Due to the sensor's measurement range in each direction, it will be difficult to install the system within the motor frame accurately, however. This chapter does not develop a mounting solution for the sensor, but rather compares the benefits and cons of different installation locations.

### ***3.6.1 Inside the motor frame***

Advantages:

- Dynamic sensing options: Higher number of variables are available for measurement enabling practical use of additional sensors.
- Immunity to environmental effects: The sensor is protected from rain and dirt when the motor frame covers it. If combined with optimal housing, only the capacitive plates are exposed to air. The frame also protects the sensor from direct physical damage and risk of theft.
- More demanding application environments: Industrial settings, such as mines and construction sites contain lots of rubble which hovers around and pollutes machines.
- Can be bundled with a motor for the customer: Saves the customer from installation trouble and from relying on an external commissioning team after supplied with a motor.

Disadvantages:

- Installation costs: The motor frame needs to be opened, after which the mounting system needs to be installed very precisely to maintain the measurement accuracies. Longer installation times, increased system downtime and possibility of more crew members increase monetary costs. If the mounting system is misaligned during the initial commissioning, additional work is required as the frame needs to be opened each time.
- Maintenance is difficult: Requires motor frame to be disassembled each time. If the sensor is not able to be split, the bearings need to be removed temporarily as well.
- Synchronizing of two separate sensors: The sensors need to be synchronized together with a communication link, which will be difficult to install within the frame when compared to linking two objects together in free space.
- Acquired measurement data is relative to the frame in a degree.
- Requires advanced mounting solution: To achieve rigidity, proper mounting casing and screws need additional application specific engineering.
- Electromagnetic interference: Might be an issue especially in inverter motors due to high IGBT switching speeds. The sensor needs to be EMI protected.

- Accessing a memory card is difficult: Unless a separate PCB design which would partially penetrate the motor frame with a card module slot, accessing a data storage card would be problematic.
- Bearing lubricant leaks: Faulty bearings spill its lubricant oil around fouling the environment. The lubricant dirties the sensor, possibly creating short-circuits between the RF circuits, and effects on the measurement results since the lubricant acts as a dielectric between the capacitive plates and the shaft surface.
- Recommissioning: Moving the sensor requires additional work once installed.
- Cabling management: Additional holes or gaps need to be drilled to the frame for the communication cables. Wireless communication becomes intriguing.
- Limited distance to bearings: If the frame is curved, a fixed width and height support plate limits the distance to the bearing.
- Circulating currents: Inverter motors contain circulating currents that flow within the motor frame. Proper grounding is a requirement.
- Higher temperatures: In the cases of overheat, the sensor has a high probability of becoming damaged due to the components maximum temperatures being generally 120° Celsius.
- Standards: Requires extremely fine-tuned mounting solution to gain true displacement values to be in accordance with vibration measurement standards.

### 3.6.2 *Outside the motor frame*

Advantages:

- Absolute measurement data: The acquired data is absolute if the support frame's footing is properly damped.
- Noise: Less noise from the other rotor end's bearing as the sensor is located at further distance.
- Sensor modification is easier: As the sensor is easily accessible to personnel, modifying it becomes effortless.
- Simpler support system design: A support system can be installed on ground
- Easy cabling: No additional design needed for managing cables.
- Installation costs:
- Synchronizing: As the cabling management is easier, connecting two sensors via physical link becomes effortless.
- Off-line monitoring: Extracting data from memory is easier.

Disadvantages:

- Limited industrial applications: As the sensor is exposed to external forces, the applications are limited to calm environments unless additional risk is tolerated.

### 3.6.3 *Mounting on drive-end*

- Noisy vibration: If measurement target is not the load, the acquired data contains noise from the load machine. The resulting data can reveal faults on the load if the equipped motor is known to be healthy, however.
- Maintenance: Detaching the sensor is difficult if the shaft is connected to an external load. Requires the separation of the two machines.
- Bearing currents: The sensor might potentially react to EMI produced by bearing currents if the current flows from the motor to the load's ground via the shaft. This current potentially shows as short-term, high frequency distortions in vibration data. The spikes must conduct directly to the data link and Ethernet adapters since the data is filtered at 3 kHz and typical bearing current frequencies are around 10 MHz (Niskanen, 2014).

### 3.6.4 *Mounting on non-drive-end*

- Coolant air temperature: Temperature of the coolant air can potentially be measured.
- Air flow: The sensor blocks the coolant air's path requiring an external motor fan.

## 3.7 CONNECTIVITY

Timestamps are convenient in condition monitoring and should be provided within data packets. EtherCAT does this automatically by adding a timestamp on received packets, so no additional functionality is required on the slave controller if data is fed continuously. However, in case of data gathered over certain time window and later sent forwards, the time cannot provide information of when the data was acquired on the system level. In these cases, including a timestamp in the EtherCAT packet separately is required on the sensor. The connection between the EtherCAT master and slave controllers is shown in the following figure (3.15).

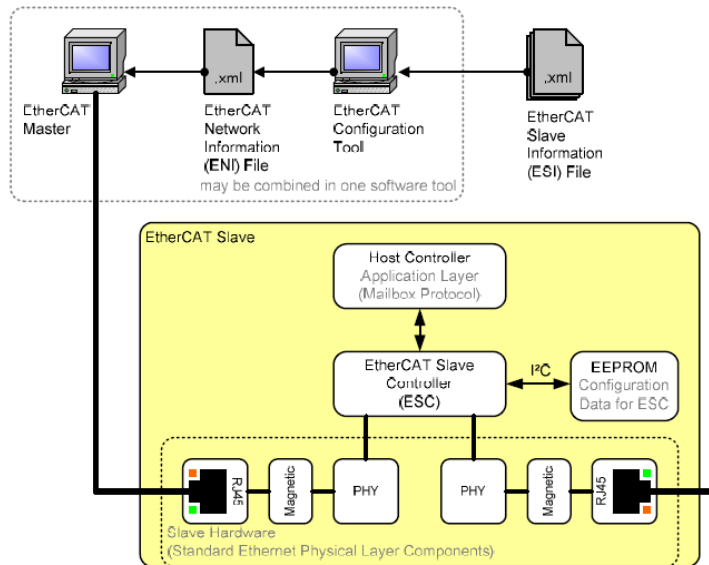


**Figure 3.15.** Connecting an EtherCAT slave controller to an EtherCAT master (EtherCAT, 2009)

The slave's EEPROM contains basic device description information. On slave boot-up, the master reads this information which enables the basic communication and control of this slave controller even if the device description XML-file is missing. However, to completely control the slave and access its extra functionalities, the XML-file must be provided.

### 3.7.1 ABB AC500-CMS PLC

The ABB AC500-CMS contains an AC500 PLC integrated with condition monitoring software and signal processing libraries. The AC500 is connected to an FM502-CMS function module, which supports up to 16 analog inputs, 50 000 samples per second data rate per channel, and 24bit ADC for each connection. 128 MB local memory enables storing of periodic data for long-term CM applications.



**Figure 3.16.** ABB AC500 CMS interface containing CPU and I/O communication modules.

As the capacitive sensor utilizes EtherCAT fieldbus for communication, a PLC module with EtherCAT support is required if no further modification is desired. CM579-ETHCAT is a communication module which contains two different EtherCAT ports for digital communication via RJ45 interface. The sensor can be connected to these ports even if the machine did not support EtherCAT protocol by utilizing the EoE property.



**Figure 3.17.** ABB CM579-ETHCAT communication module.

At the facility, the AC500-CMS is connected to a COM600 industrial computer that controls a VFC connected to a rotating device, as seen in figure 3.18 below. The COM600 is connected to ABB's cloud service "ABB Ability", which enables inspection of data remotely.

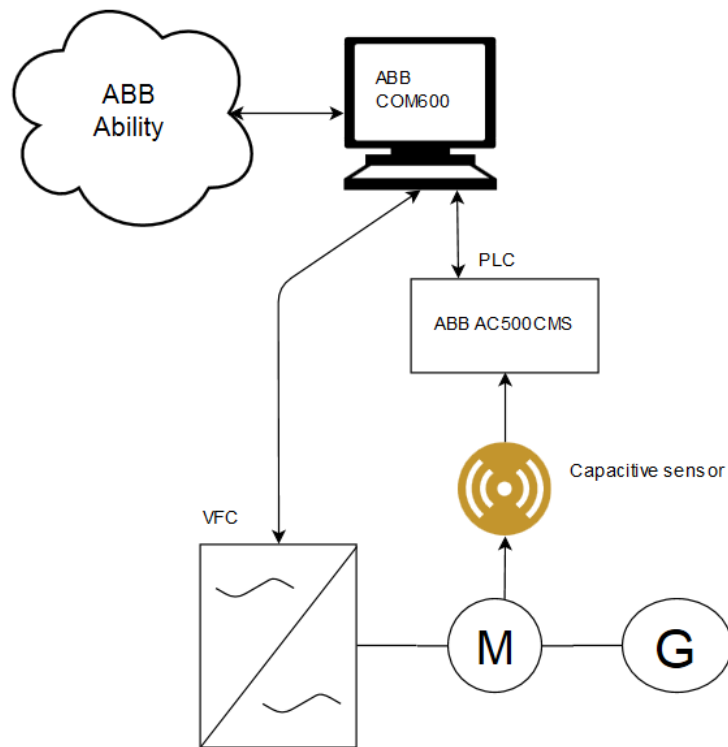


**Figure 3.18.** A block diagram of ABB’s proposed environment.

The connection of capacitive sensor has been tested successfully on an AC500. The AC500 programming software, ABB Automation Builder only requires the device description .XML-file to access the sensor process data. However, AC500’s minimum cycle time of one millisecond limits the EtherCAT communication rate to 1000 Hz. To transfer, for example 10 kHz data from the sensor, a buffer of 10 samples should be sent instead of every sample separately. The sensor is modified to convert 20 kHz data rate into a millisecond cycle time by oversampling the data by 20 samples and sending these samples as a buffered packet every 1 millisecond. No timestamps are available for the data, but for data visualization, the data points are separated by 50 microseconds.

Additionally, the CM579 module’s maximum quantity of input and output data is 5760 bytes. By assuming the outputs are not used, the amount of 16-bit samples is 2880. If the PLC program contains pre-existing code, there is a possibility that the CPU is not able to run the program within its predetermined cycle time. A buffer size of 2880 bytes is possible to be implemented on the sensor, which equals a time sweep of 0,144 seconds which also reduces the timing cycle time constraints on the PLC. However, the maximum number of sensors connected to each other via line structure becomes limited to 72 if the sensors are sending 20 samples from each axes every millisecond. Theoretically, 36 machines are measurable in real time if each of them is equipped with two sensors, each on drive and non-drive ends.

A descriptive picture of configuring the capacitive sensor on Automation Builder 2.0 is presented in the following figure (3.19).

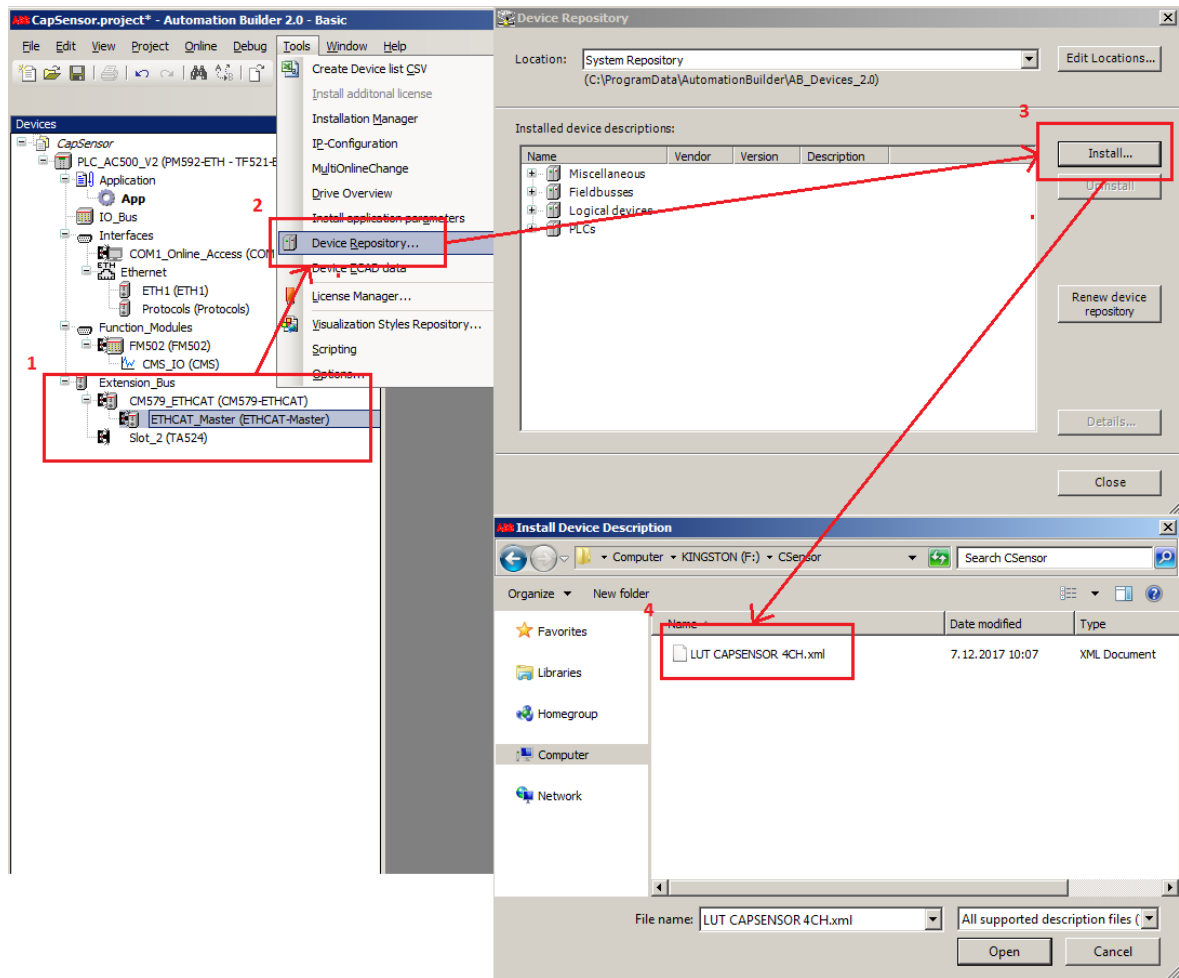


**Figure 3.19.** Configuring the capacitive sensor on ABB Automation Builder 2.0.

Firstly, the configuration requires an EtherCAT master module to be added to the extension bus. After the device description .XML file is installed and added to the project, the sensor can be added to the project under the right-click menu of the EtherCAT master. The sensor's X and Y axes' data can be accessed instantly after assigning the values from the EtherCAT process data objects to project variables.

The following table shows differences of digital and analogue connections. The EtherCAT shows plenty of advantages over analogue connection and the digital transmission would be generally more favorable as long as the sensor is accompanied with a computer with Ethernet adapter. The analogue connection is favorable in situations without a digital transmission possibility.

**Table 10.** Comparison between digital and Analogue 4...20 mA connectivities.

Subject	Connection type	
	Digital	Analogue 4...20 mA
Interference	Highly resistant to EMI and RF	Cables require EMI shielding
Resolution	16-bit ADC, 16-bit EtherCAT	24 bit (AC500-CMS)
CPU	Required	Not required
Bandwidth	100 Mbit/s (EtherCAT standard speed)	Cable and sampling rate limited. 50 000 samples per second sampling rate on AC500-CMS
Complexity	Line topology enables connecting several sensors to master in serial	Requires analogue wiring for each channel
Data compression	Possible	Complex
Maximum cable length	100 m (copper), > 2 km using fiber optics without repeaters	100 m
Cost	One Ethernet cable	Four analogue cables
Connectivity	Almost any computer	Analogue inputs

### 3.7.2 *Other computers*

It has become clear from previous chapter (3.3) that the sensor is not limited to only industrial computers. The limiting factor is the hardware requirement of implementing an EtherCAT master. Most of the supported network adapters and chipsets are listed in (Etherlab, 2018), (Beckhoff, 2018). EtherCAT master and slave implementations are also available as open source and are available publicly on the web.

### 3.7.3 *Master topology*

The sensor has several choices to upload its data to. AC500-CMS, normal PCs and even modern VFCs such as ACS880 series can be programmed to receive and save data from external sensors. The AC500-CMS and ACS880 require storage unit if data was to be kept over longer periods as they do not contain permanent storage built into them. AC500 can be supplied with an SD-card, however, and ACS880 requires an ABB's NETA-21 datalogging module to save data.

### *3.7.3.1 To AC500-CMS*

The machine requires 1 millisecond cycle time in order to receive coherent data from the sensor and the sensor must contain corresponding oversampling factor programmed in it. The PLC might not keep up with its configured cycle time if the programmed software is complex and therefore containing plenty of instructions. Thus, the PLC must be assigned almost completely to light programs if it is supposed to be used as data acquisition tool. However, by increasing the number of oversamples on the sensor, the cycle time requirement can be reduced, and possibly complex software is possible to be run along with the sensor. An SD-card is required if the data is desired to be stored locally, or an external computer to send the data to via Ethernet connection.

### *3.7.3.2 To COM600*

Installing an EtherCAT master software is a prerequisite to acquire data from the sensor. The open source implementation requires Windows2000 to Windows 7 operating system. The COM600 is shipped with Windows 8 and the support for EtherCAT is not tested but is stated as “might work” (SOEM, 2015). The solution will require testing in practice to state the applicability. A direct data path into the COM600 seems like a feasible solution as the computer’s purpose itself is already to work solely as a database system. The computer is also connected to ABB’s cloud service, which makes post forwarding the data easy. Additionally, as seen in figure 3.18, less middleware would be required by removing the need of a data logging PLC and thus lessening the costs and setup complexity. Also, as the computer runs Windows 8, possibly external data processing tools are already available, and the development of personal software is possible.

### *3.7.3.3 To ACS880*

The ACS880 requires FECA-01 EtherCAT adapter installation to the VFC. A NETA-21 module or a separate computer is required to save the acquired data. The minimum cycle time of an ACS880 is 1 millisecond as well and therefore requires a data buffer on the sensor.

## 4 LABORATORY TEST-SETUP

The sensor is tested in LUT electrical machine laboratory. The sensor is mounted on an ABB 3-phase M3BP 160 MLA 4 motor and connected to a Beckhoff EK1100 EtherCAT master that is connected a Beckhoff PLC via EtherCAT (figures 4.1 & 4.2). The motor is controlled using an ABB ACS800 VFC. The sensor was powered by Phoenix Power TRIO-PS/1AC/24DC/2.5 AC to DC converter that was connected to a 230 V AC power supply. The sensor's distance to the bearing housing is 26 mm. The sensor was mounted on three screws and secured in place with knobs, and no separate isolation and damping according to measurement standards was used in prototype testing. The mounting system was not calibrated with micrometer accuracy which must be considered with offset compensation.



**Figure 4.1.** Capacitive sensor mounted on an unloaded motor.

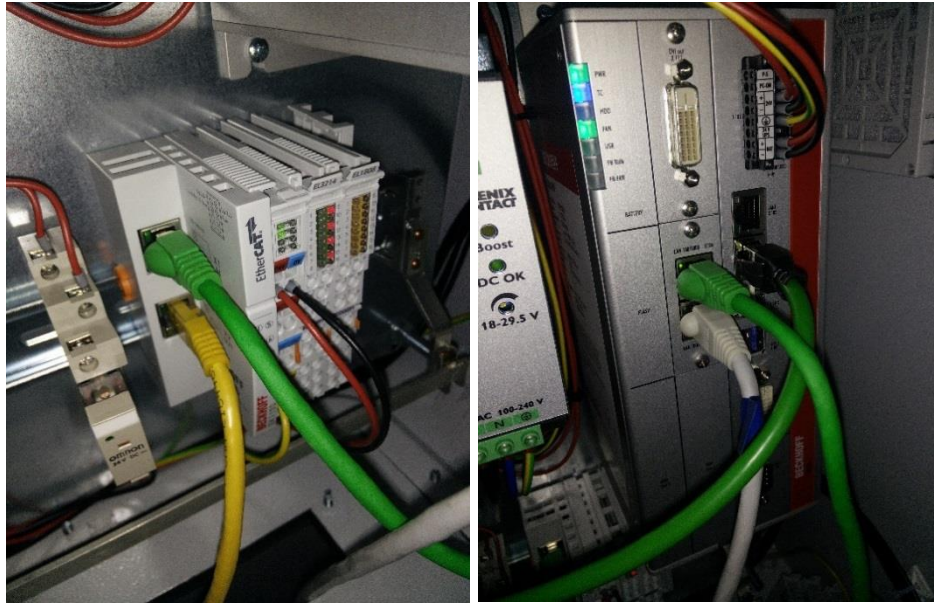


**Figure 4.2.** EtherCAT connection of the sensor to EK1100 (left, green cable) that is connected to the Beckhoff PLC (right).

First, the motor was driven from zero speed to 1500 rpm with no load (figure 4.3). The data from the capacitive sensor was digitally filtered using a Simulink IIR low-pass filter with 2 kHz passband frequency and 3 kHz stopband frequency. The capacitive sensor's positive and negative channels are summed together to produce absolute X and Y distances. At  $t = 3$  s, a speed reference  $n = 1500$  rpm was given to the VFC. The VFC starts magnetizing the motor which results in forces acting on the rotor which the capacitive sensor can sense. At  $t = 7$  s the motor starts to accelerate until 13 second mark after which the VFC was given a stop command. The VFC stops supplying current and the motor enters a freewheeling state until it reaches zero speed at 27 second mark. The results show that the acquired displacement data is very detailed. The figure 4.4 contains a zoom of the capacitive sensor's data. The initial offsets are post processed to 0  $\mu\text{m}$ .

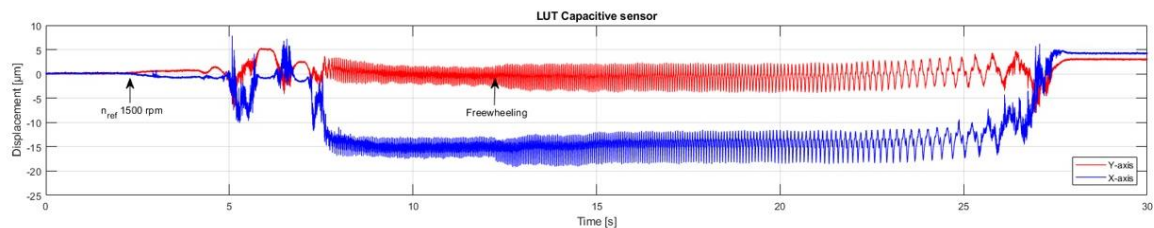


**Figure 4.3.** Capacitive sensor data with no system load,  $n_{\text{ref}} = 1500$  rpm.

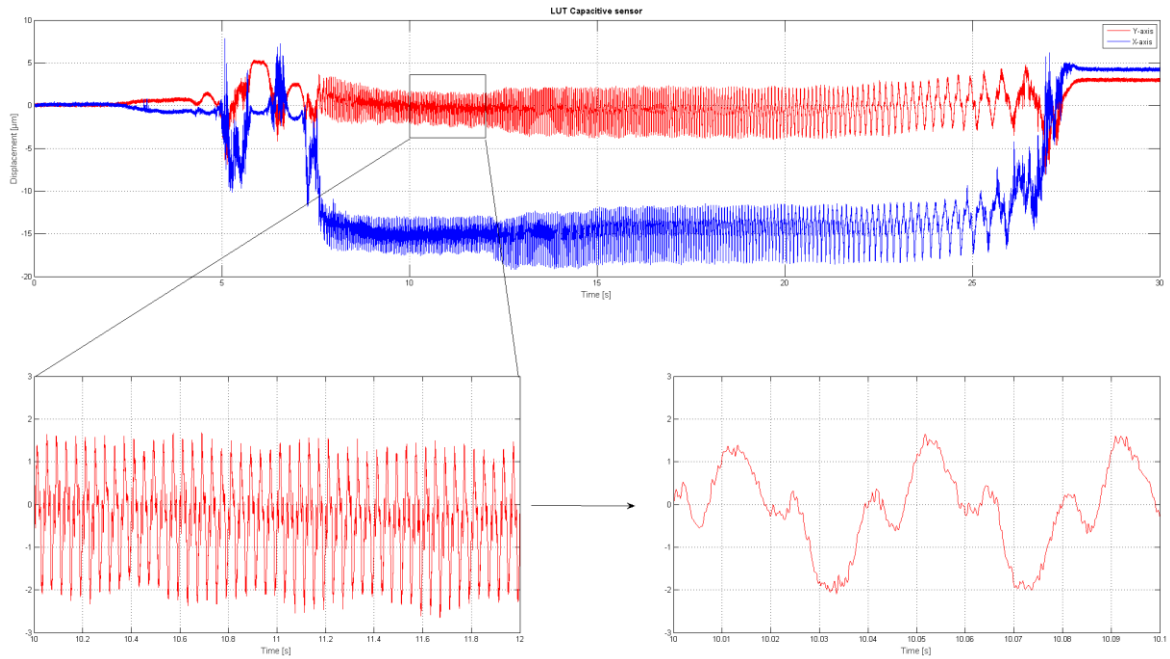


**Figure 4.4.** A closeup of the capacitive sensor data.  $n_{ref} = 1500$  rpm.

The data content of both X and Y axes are similar and thus only one of them are shown in the figure. Clearly, the sensor can measure distances very accurately. From the most zoomed in picture, the motor speed is possible to be calculated. Visual inspection shows that the rotor spins one turn in 0,04 seconds which yields exactly in 25 Hz frequency. The sensor could therefore be used as an indirect speed estimator with a correct algorithm.

Next, the motor was loaded with a coupling hub that weighs 3,5 kg, measured with an A&D EK-12KA multi-function compact balance. The coupling hub was equipped with a screw and knobs to produce unbalance to the system.

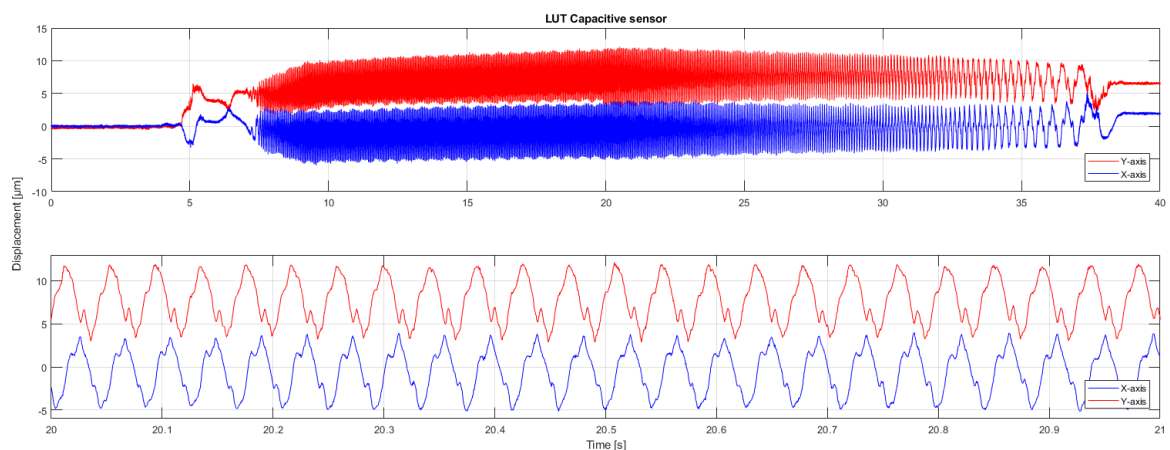


**Figure 4.5.** Speedup from zero state to 1500 rpm with the system loaded with gear and unbalance.

Due to the extra mass, the rotor is heavier and reacts less to the magnetizing forces during the VFC's magnetizing phase. The displacement amplitudes in both axes are risen from

roughly  $4\ \mu\text{m}$  (no load) to  $9\ \mu\text{m}$  (load) peak-to-peak. The offsets at  $t = 37\ \text{s}$  are suspected to be due to warming of bearing lubricant.

The effect of magnetizing forces is shown in the following figure. The magnetizing forces were produced by setting the speed reference to zero rpm and starting the VFC.

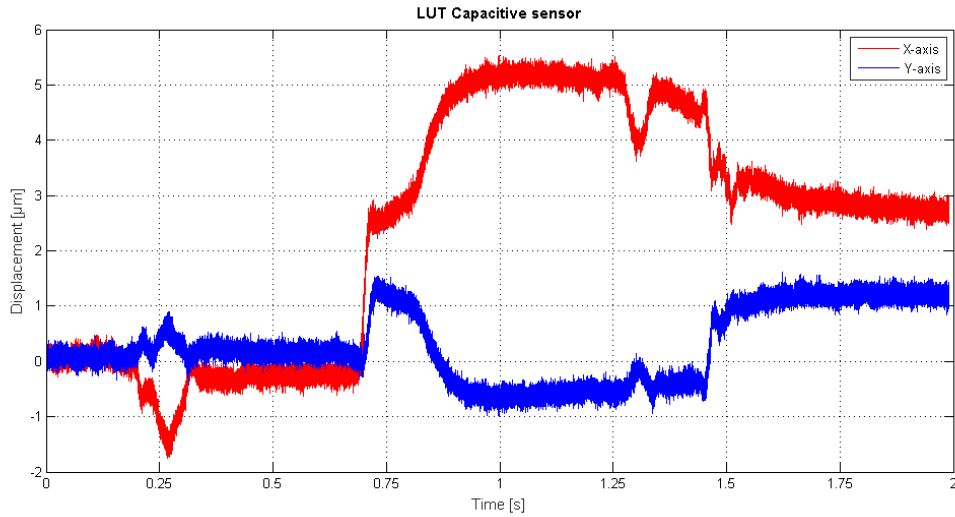


**Figure 4.6.** The effect of magnetizing forces on the rotor displacement.

The motor was also connected directly to the 50 Hz grid to produce the extreme forces at the system power up. The system was firstly connected with no load. The following figure shows that the displacement peak in the system startup is clearly visible. The average displacement of both axes is also closer to each other during steady state.

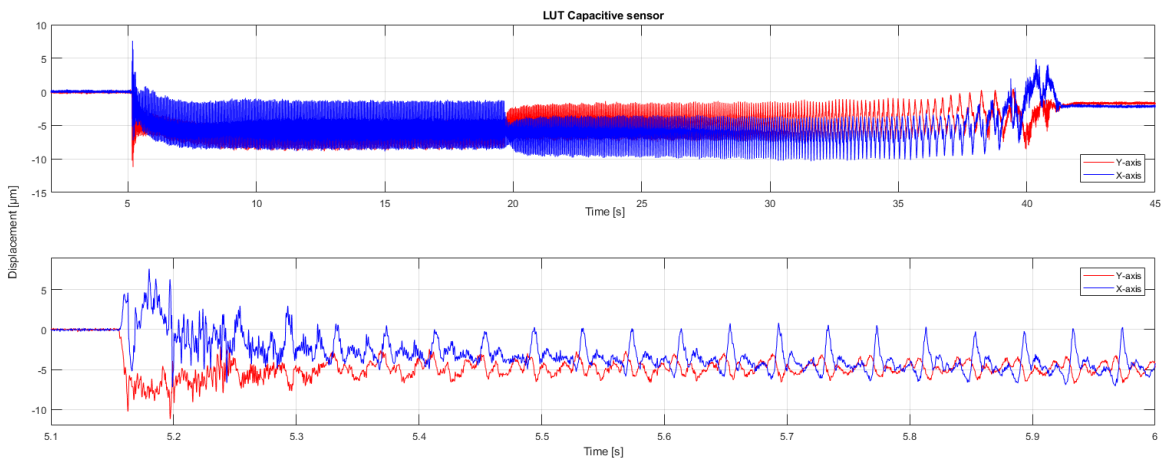


**Figure 4.7.** Unloaded motor connected directly to 50 Hz grid.

Afterwards, the motor was connected to the same 50 Hz grid voltage but with the identical coupling half and unbalance as earlier. The figure 4.8 below shows that the initial peak rises from  $10\ \mu\text{m}$  to  $30\ \mu\text{m}$  peak-to-peak when there exists extra load and unbalance. Additionally, the average displacements of both axes during runtime are nearly identical with the initial state ( $t = 0\ \text{s}$ ).

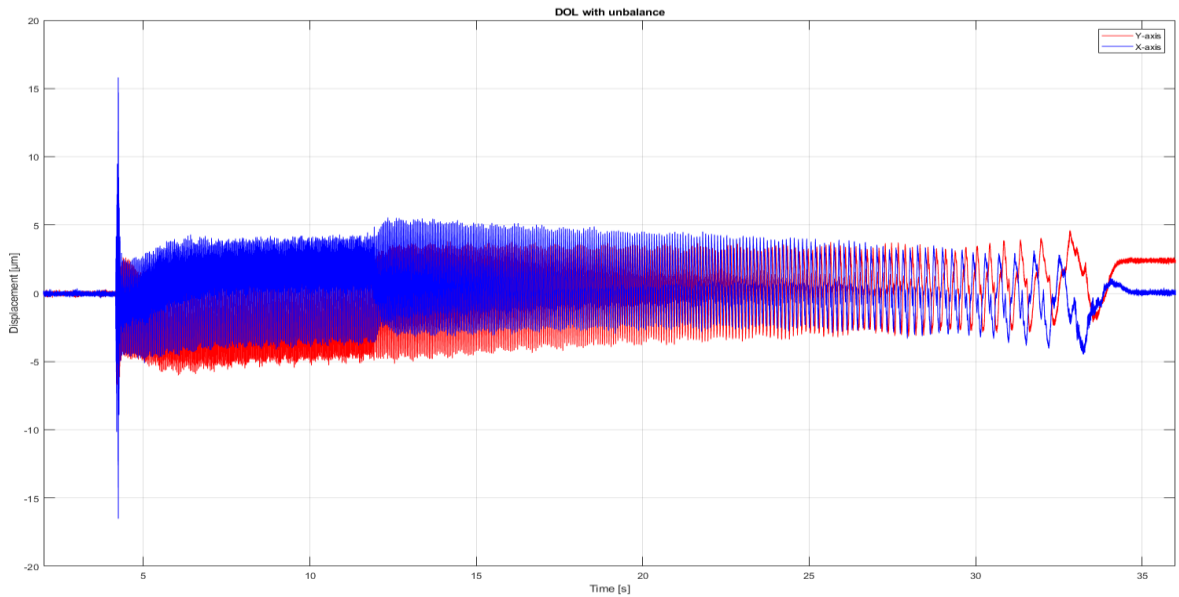


**Figure 4.8.** Motor loaded with gear and unbalance connected directly to 50 Hz grid. DOL stands for “Direct On Line”.

Furthermore, the following XY-graphs were obtained. The figures present a virtual axial center trails. The figures contain 40 Hz low-pass filtered as well as previously used 2 kHz low-pass filtered data sets over 6000 samples. The 1X filtered data shows a typical looking circular trail which might often imply a correctly behaving machine. \

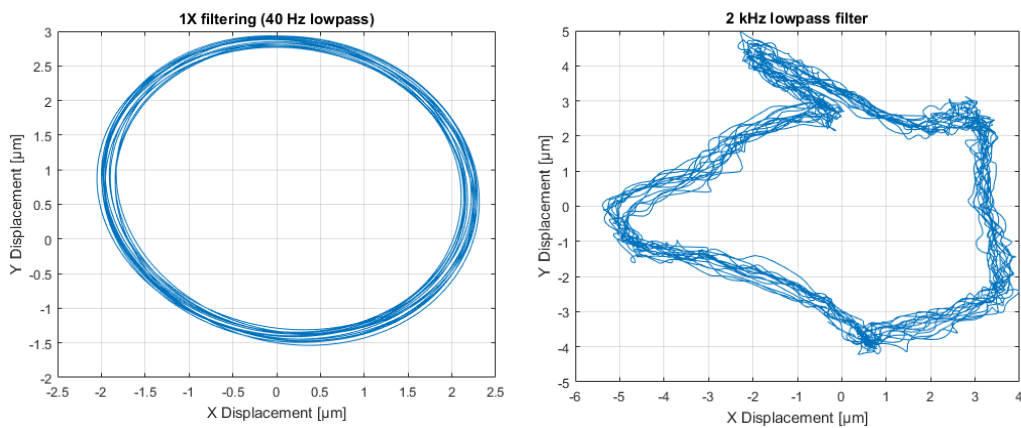


**Figure 4.9.** 40 Hz and 2 kHz low-pass filtered XY-orbital plots over 6000 samples.

Interestingly, however, the 2 kHz filtered graph reveals major different shapes. The shape is far from circular, and some spikes are present in the upper part of the orbit. At lower speeds, a 2 kHz filtered orbital figure contains sharper corners as seen in the following figure.

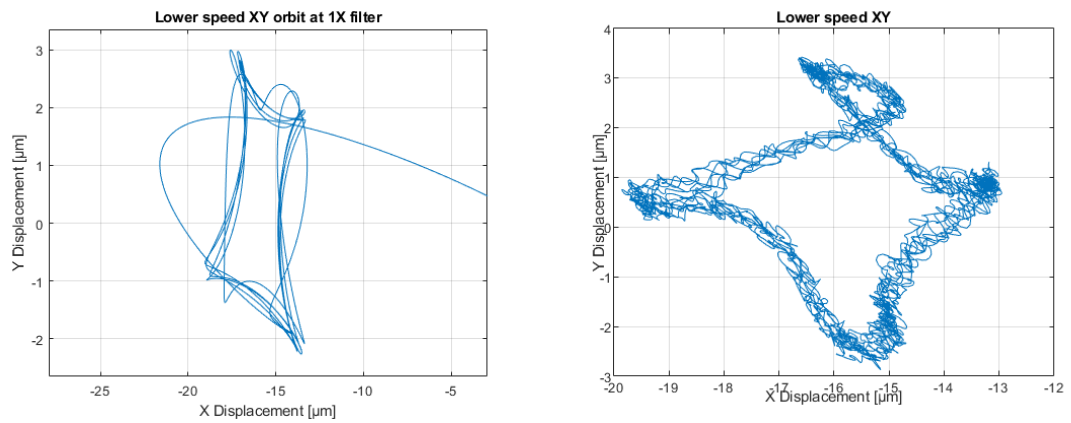


**Figure 4.10.** XY orbital plot over 6000 samples at lower rotational speed. 40 Hz low-pass filtered data on the left, 2 kHz on the right.

Moreover, FFT of the grid connected cases (unloaded and unbalanced) are also presented as the clean sine wave environment provides comparable data. The time periods selected represent the rotor spinning at nominal frequency. The signals were plotted and presented using Matlab and 20 kHz as the sampling rate option. The frequency axis is limited to 500 Hz as it was noted that no amplitudes were present above the selected limit.

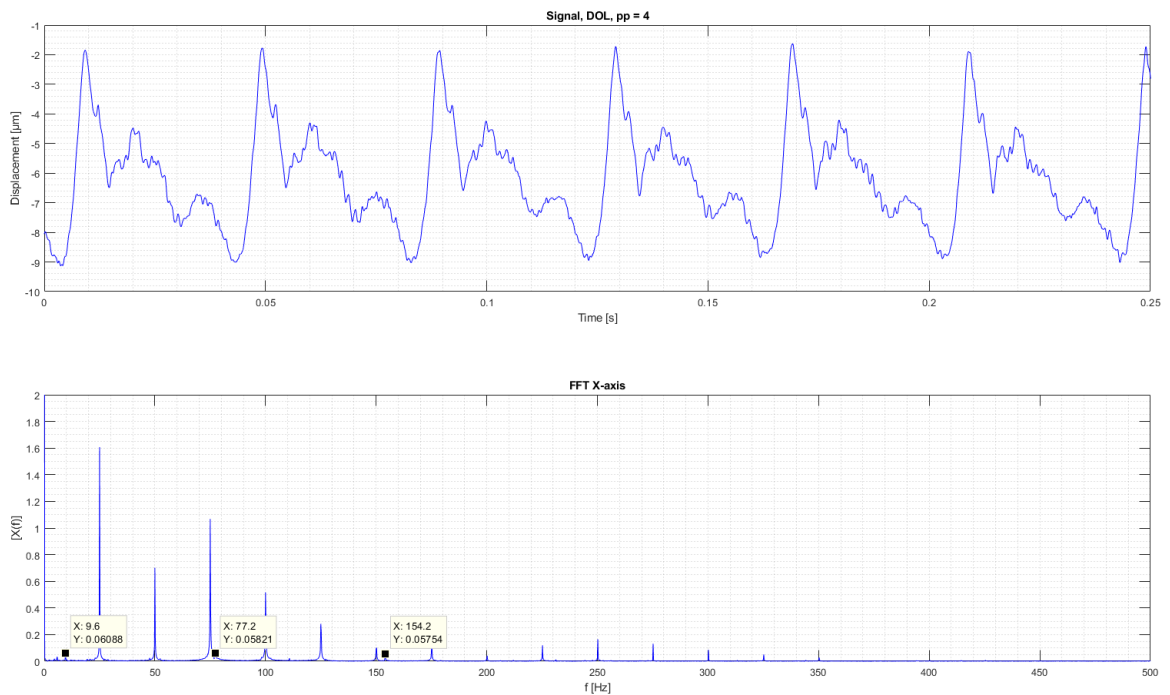


**Figure 4.11.** FFT of 50 Hz grid connected unloaded motor X-axis.

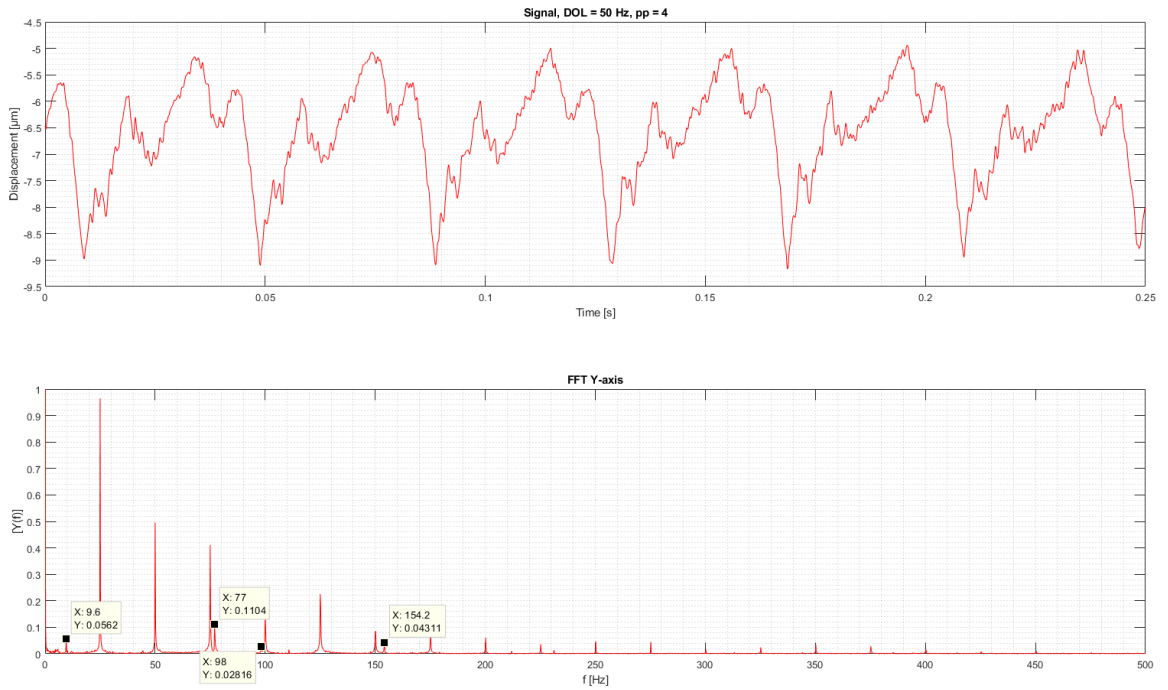


**Figure 4.12.** FFT of 50 Hz grid connected unloaded motor Y-axis.

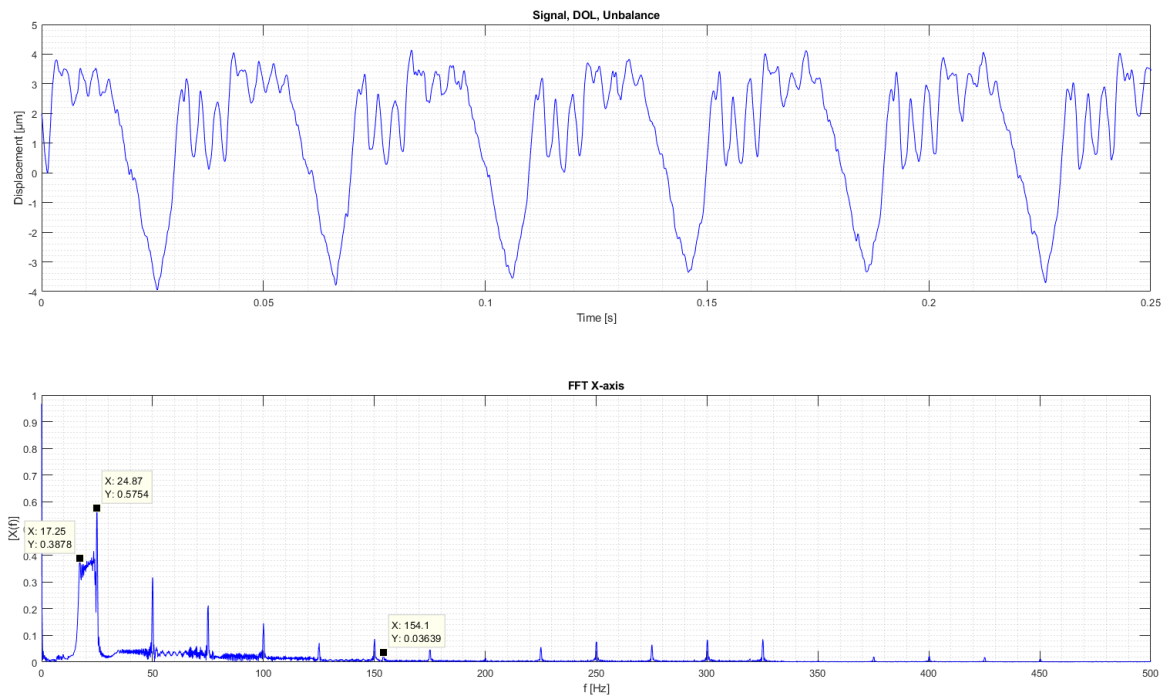


**Figure 4.13.** FFT of 50 Hz grid connected loaded and unbalanced motor X-axis.

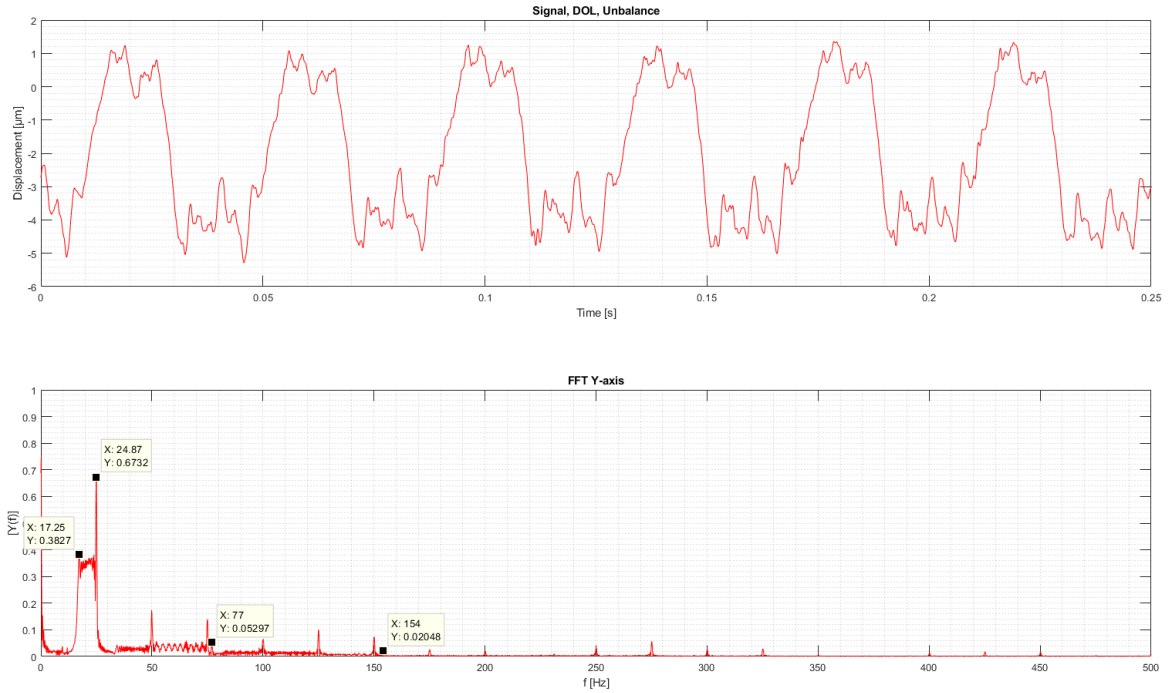


**Figure 4.14.** FFT of 50 Hz grid connected loaded and unbalanced motor Y-axis.

The unloaded motor FFT shows mainly harmonics of the rotor spin frequency and can be thought as working normally. The unbalanced motor, however, displays extreme shapes near the rotor speed as well as other odd behavior near 50 Hz. Clearly, the unbalance is detectable.

The motor bearings in the setup were 6309 for the drive end and 6209 for the non-drive end. The bearing dimensions and frequencies using the equations (4-7) are listed in the table below (NTN, 2010).

**Table 11.** Laboratory motor’s bearing dimensions and their corresponding frequencies at  $n = 1500$  rpm/min.

Bearing	$NB$	$BD$ [mm]	$PD$ [mm]	$\phi$ [°]	$BPFO$ [Hz]	$BPFI$ [Hz]	$FTF$ [Hz]	$BSF$ [Hz]
6309	8	17,4	7,4	0	76,4	123,6	9,6	50,1
6209	9	12,7	6,5	0	90,5	134,5	10,1	61,5

By comparing the bearing frequencies to the frequencies seen in the FFT of unloaded motor, it is noted that the frequencies are similar to the rotor speed frequency’s harmonics. As the peak levels at these frequencies seem similar with each other and no noticeable abnormalities are detected, the bearings are most likely in good condition. The non-drive end bearing frequencies most likely do not show up in the graphs as the distance between the sensor and this bearing is over 0,4 meters. By prior knowledge, the setup’s bearings did not have addressed to contain any damage. However, the 50 Hz unloaded motor X-axis shows a small peak at the exact FTF value of the drive-end bearing which might imply correlation between each other. The loaded motor might mask bearing frequencies as the overall level seems to be risen. Future work will be required to identify whether artificially created bearing faults result in differences in the FFTs.

Additionally, an algorithm for speed estimation (figure 3.13) was tested in practice but a separate Simulink model found to be working better as it was also faster to develop and debug on the fly. The following figure shows the estimated speed from  $n = 150$  rpm to 1500 rpm after which the power was turned off manually, letting the motor stop by itself. The input frequency was manually risen by the user by holding down the speed reference button down until the electrical frequency reached 50 Hz. A low-pass filter with cutoff frequency of 25 Hz was used in the model.

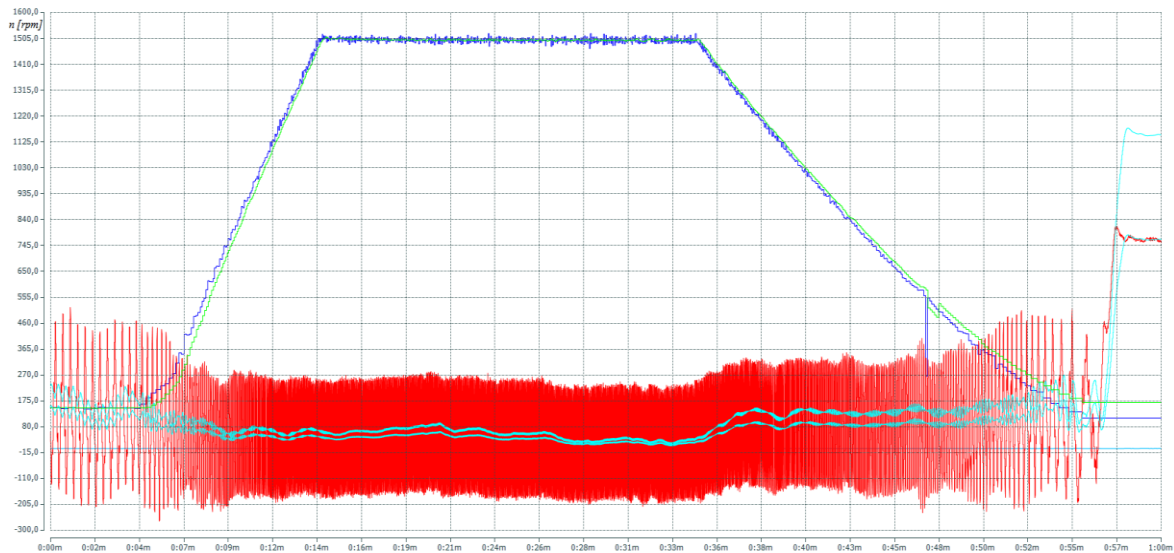


**Figure 4.15.** Speed estimation based on vibration signal. Blue signal represents the raw speed estimation, green its averaged median values, teal colors are the dynamic upper and lower limits the algorithm is based on and red is the vibration data of Y-axis. The scale for vibration is irrelevant.

The Simulink speed estimator has been tested to produce speed estimations correctly above 120 rpm, or 2 Hz mechanical rotational speed. As the model is based on band-cross algorithm, equivalent of zero-cross detection, the frequency is calculated on the vibration signal crossing the teal colored lines. At lower speeds the vibration becomes chaotic and the estimator does not produce accurate values.

#### 4.1 CONCURRENT USE OF TWO SENSORS

Two newly constructed sensors were also demonstrated in practical use in the laboratory. Similar test setup was used as before but by having two sensors located on the same mounting frame, 26,8 mm apart from each other. The sensors were supplied with two separate, isolated power supplies that were connected to the same socket. They were connected to the Beckhoff industrial computer via single Ethernet cable using line structure.

During the measurements, both sensor noise levels were gradually increasing even under motor steady state. The noise increased slowly from 0 to 50  $\mu\text{m}$ . In the case where the system had an older sensor next to a newer one, the older sensor expressed less noise than in the setup of two newer sensors. It is considered that the sensors' resonance circuits might

conduct to each other as both use the same surface for measurement. By moving the sensors further apart, the noise also decreased. As the resonance frequency of the sensors are 430 MHz, the wavelength of the electric signal is

$$\lambda = \frac{c}{f}, \quad (26)$$

where  $\lambda$  is wavelength and  $c$  is the speed of light. The wavelength of the resonance circuit results in 0,69 m. It is a strong implication of conductivity via the shaft as the sensors were placed together at the third of the wavelength. To further explore the causes, the sensors need to be shielded and placed further apart. The new sensors also contained some hand-soldered parts that differ from the original design slightly which might also effect on the result. However, all of the sensors functioned as desired under single sensor measurements, but the newer sensors clearly had more noise.

## 5 ABB PRACTICAL DEMONSTRATION

A demonstration was successfully presented at Helsinki. The system consisted of the sensor equipped on a brand new 7,5 kW ABB M4AA 132 three phase, four pole asynchronous motor that was connected to an oil pumping system. Unfortunately, the pump's nameplate was not available at the time. The motor was controlled using ABB SAMI GS frequency converter. The demonstration motor's shaft surface roughness was measured using Obsnap TR100 surface roughness tester resulting in the value of  $1,2 \mu\text{m}$ .



**Figure 5.1.** Demonstration setup.

The sensor was connected to an AC500 PLC, which consisted of a PM582-ETH CPU and a CM579 EtherCAT module. The system was run at electrical frequencies of 20, 30, 40 and 50 Hz. The data was saved to a 1 GB SD-card directly from the AC500. The limited internal memory of the older version CPU forced slightly shorter recording times. The acquired data sets contain data over 2,5 seconds even though the plan was to gather data over three seconds. The acquired data is sampled at 20 kHz without any filtering. The data is visualized using Matlab. The X and Y axes' signals and FFTs of 20 and 50 Hz electrical supply frequencies are presented in the following figures (5.2 & 5.3). The initial offsets are manually removed from the signals for easier comparison between both axes. The expected bearing frequencies are also presented in the upcoming tables at their respective velocities. It should be noted

that the load presents slip, which in turn effects on the rotor speed and therefore on the bearing frequencies being slightly lower in practice.

**Table 12.** Demonstration motor's bearing dimensions and their corresponding frequencies at  $n = 600$  rpm/min.

Bearing	$NB$	$BD$ [mm]	$PD$ [mm]	$\phi$ [ $^\circ$ ]	$BPFO$ [Hz]	$BPFI$ [Hz]	$FTF$ [Hz]	$BSF$ [Hz]
6208	9	11,89	59,99	0	36,1	54,0	4,0	24,2
6206	9	9,53	46,48	0	35,8	54,2	4,0	23,4

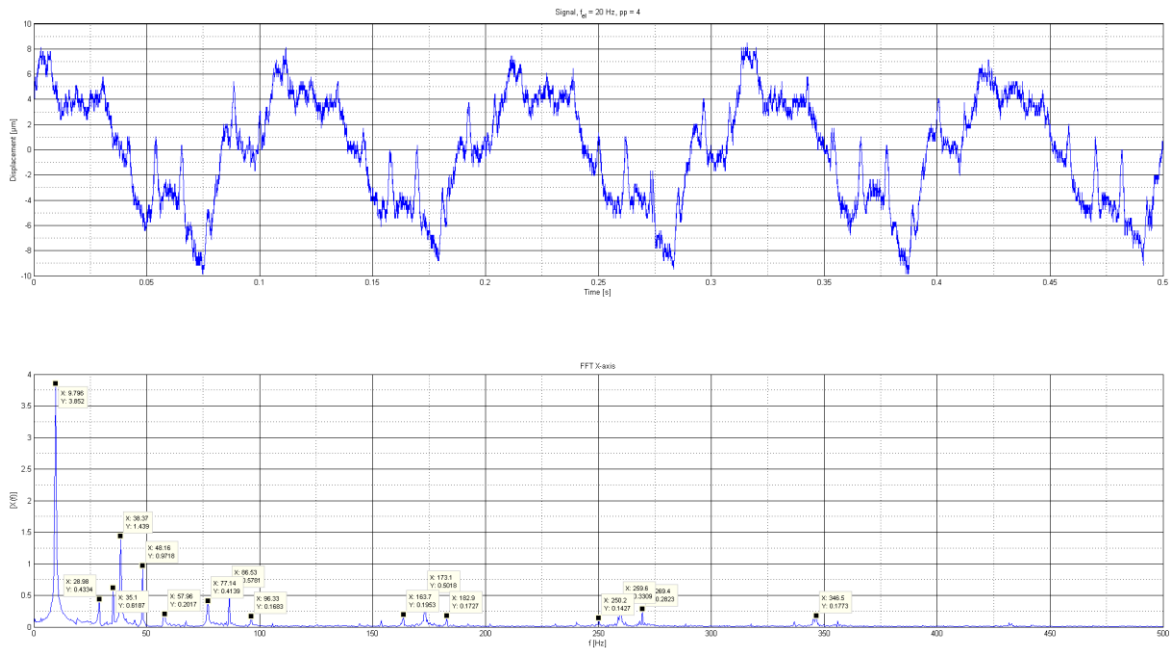


**Figure 5.2.** 20 Hz X-axis signal and FFT.

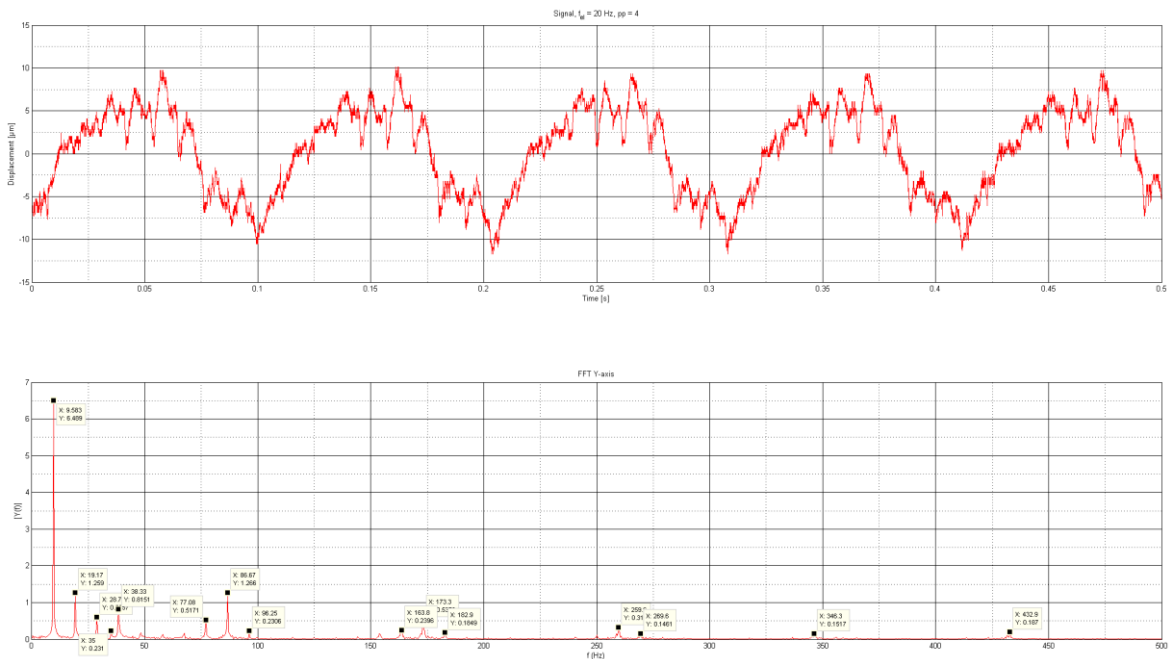


**Figure 5.3.** 20 Hz Y-axis signal and FFT.  $f_{e1}$  is the electrical frequency and pp is the number of poles.

Both axes show a small peak at  $f \approx 35$  Hz. It can be concluded from the figures that the frequency is not a harmonic of the slip speed as it is not a multiple of 9,59 Hz. The 35 Hz frequency also falls near to the BPFO frequencies shown in the table 12. The BPFO of the 6208 bearing at this slip speed is 34,6 Hz and the drive-end bearing most likely is only seen in the signal as the sensor is mounted on the drive end. Other harmonics might be a result from the pump impellers and shaft unbalance as they are multiplies of the rotating speed. The other nominal bearing frequencies might be present but they cannot be distinguished from the main harmonics. The data acquired at  $n = 1500$  rpm is shown in the following figures and the corresponding calculated bearing frequencies are also presented.

**Table 13.** Demonstration motor's bearing dimensions and their corresponding frequencies at  $n = 1500$  rpm.

Bearing	$NB$	$BD$ [mm]	$PD$ [mm]	$\phi$ [ $^\circ$ ]	$BPFO$ [Hz]	$BPFI$ [Hz]	$FTF$ [Hz]	$BSF$ [Hz]
6208	9	11,89	59,99	0	90,2	134,8	10,0	60,6
6206	9	9,53	46,48	0	89,4	135,6	9,9	58,4

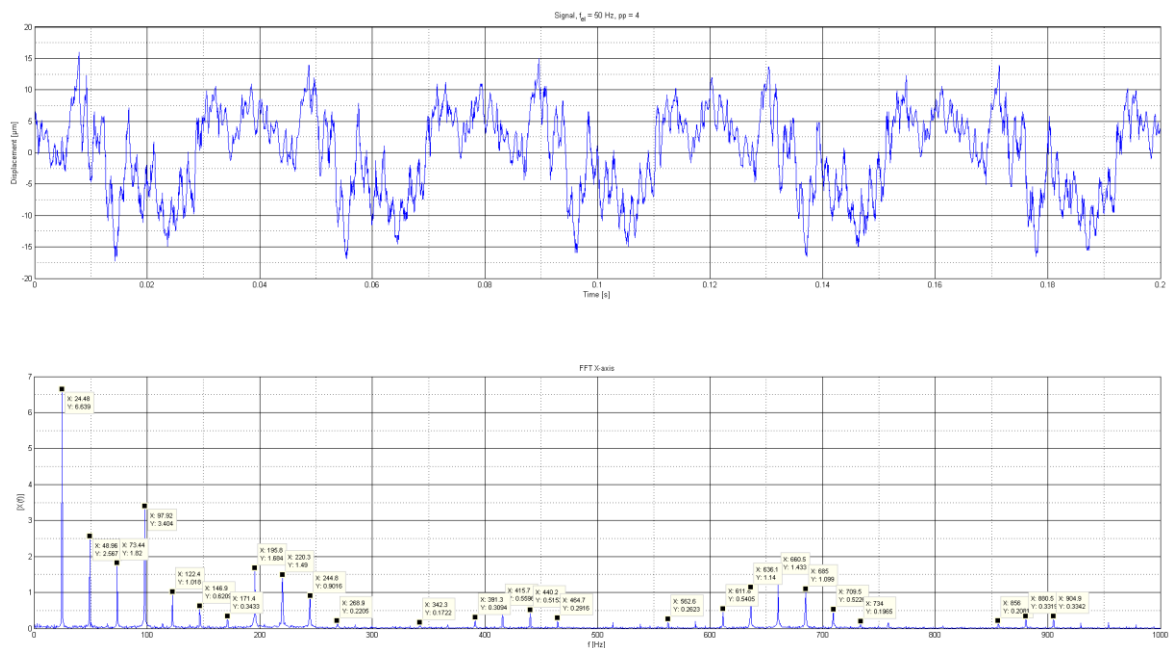


**Figure 5.4.** 50 Hz X-axis signal and FFT.  $f_{el}$  is the electrical frequency and pp is the number of poles.

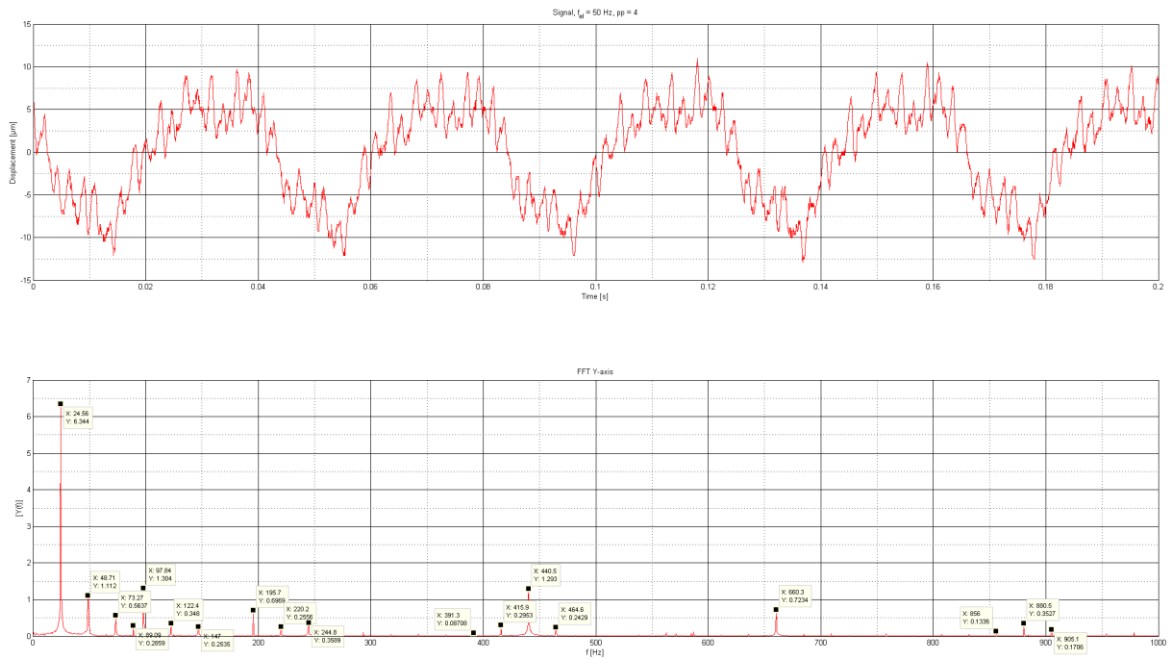


**Figure 5.5.** 50 Hz X-axis signal and FFT.

The actual motor speed from the FFT is the highest peak and is 24,56 Hz which results from the motor slip. The fourth peak in the Y-axis FFT shows a value of 89,09 Hz which falls within 1 % band of the corresponding BPFO nominal frequency of both bearings. It is likely that this frequency is a result from the bearing outer cage. The higher frequencies may be the result of motor's resonances. The rotor exhibits harmonics at the rotor speed multiplies  $f_r \pm kf_r$ , where  $k$  is an integer.

## 6 SUMMARY AND CONCLUSIONS

Condition monitoring is an extremely large area of research in electrical machines as it consists of several different research zones. A key element of condition monitoring in rotating machines is the rotating shaft. Radial forces on the motor shaft results in odd behavior, and bearings often are the first element to break due to this. If the fault has undergone undetected for a long period, the system might come to a sudden halt resulting in major expenses and unexpected downtimes. The industry has several different tools used in identifying faults using different condition monitoring strategies that are based on different physical phenomena, such as measuring shaft displacement, stator electric currents, system sound levels and temperatures, for example.

In this thesis, the three-axis capacitive sensor has been successfully proven to be able to detect beneficial phenomena in condition monitoring and the data acquisition has also been enhanced to support connectivity to end-user systems. Some ideas for further development is also proposed. The sensor mounting solution needs to be so that it contains enough damping from the motor frame. The sensor needs to be shielded from electromagnetic interference as well as radio frequency noise. An alternate design on the physical dimensioning is required in order to make commissioning easier. An alternate digital board needs to be developed and therefore additional features are addable. Connecting external sensors to the board is also possible after some circuit development. The current connectivity to external devices has been found extremely suitable currently, as it is possible to be connected virtually to any modern PC. Wireless connectivity is also an area of interest.

The laboratory measurements present interesting data as they strongly imply that the sensor might detect bearing faults at some level. As this work is not intended to contain deep condition monitoring analysis, future work will be required and knowhow from the professionals. Research on faulty bearings, faulty sprockets and gears as well as magnetic unbalance detection will be areas of interest. Nowadays, as frequency converters are more and more common, the risk of bearing and shaft currents also are higher. It is also interesting if the bearing and shaft currents have an effect on the sensor and if the sensor data can pinpoint the phenomenon.

Further advancement of algorithms is required as the raw data acquired in laboratory is extremely promising. For example, the acquired data is clear enough that the rotor rotating speed can be estimated and better algorithms are needed for lower speeds. Additionally, the sensor integration to ABB's cloud services will be requiring future work.

## REFERENCES

- (ABB, 2017) ABB Automation Products GmbH, “Frequency Asked Questions”, 2018. Accessed on 2.10.2017. Available at: <http://new.abb.com/motors-generators/service/advanced-services/remote-condition-monitoring/faqs>
- (ABB, 2017) ABB Automation Products GmbH, “FM502 Function Module datasheet”, 2018. Accessed on 21.5.2018. Available at: <https://search-ext.abb.com/library/Download.aspx?DocumentID=3ADR010027&LanguageCode=en&DocumentPartId=&Action=Launch>
- (Analog Devices, Inc., 2017) Analog Devices, ADT7312 Temperature Sensor datasheet. Accessed on 21.5.2018. Available at: <http://www.analog.com/media/en/technical-documentation/datasheets/ADT7312.pdf>
- (Beckhoff, 2015) Beckhoff Automation GmbH & Co., ”EtherCAT Slave Controller IP Core for Xilinx FPGAs release 3.00k”, Hardware Description, 2015. Accessed on 27.11.2017. Available at: [https://download.beckhoff.com/download/document/io/ethercat-development-products/ethercat\\_ipcore\\_xilinx\\_v3\\_00k\\_datasheet\\_v1i0.pdf](https://download.beckhoff.com/download/document/io/ethercat-development-products/ethercat_ipcore_xilinx_v3_00k_datasheet_v1i0.pdf)
- (Beckhoff, 2018) Beckhoff Automation GmbH & Co., “Supported Network Controller by Beckhoff Ethernet Driver”. Accessed on 21.5.2018. Available at: [https://infosys.beckhoff.com/english.php?content=../content/1033/tcsystemmanager/reference/ethercat/html/ethercat\\_supnetworkcontroller.htm&id](https://infosys.beckhoff.com/english.php?content=../content/1033/tcsystemmanager/reference/ethercat/html/ethercat_supnetworkcontroller.htm&id)
- (Chen, 1998) S. Chen and T. A. Lipo, “Bearing Currents and Shaft Voltages Of An Induction Motor Under Hard- And Soft-Switching Inverter Excitation”, *IEEE Trans. Ind. Appl.*, vol. 34, no. 5, pp. 1042–1048, Sep./Oct. 1998.
- (EtherCAT, 2009) EtherCAT Technology Group, “EtherCAT Slave Implementation Guide”, 2012. Accessed on 21.5.2018. Available at: [http://www.ethercat.org/pdf/english/ETG2200\\_V2i0i0\\_SlaveImplementationGuide.pdf](http://www.ethercat.org/pdf/english/ETG2200_V2i0i0_SlaveImplementationGuide.pdf)
- (Ethercat, 2014) EtherCAT Technology Group, “Industrial Ethernet Technologies: Overview”, 2014. Accessed on 21.5.2018. Available at: [https://www.ethercat.org/download/documents/Industrial\\_Ethernet\\_Technologies.pdf](https://www.ethercat.org/download/documents/Industrial_Ethernet_Technologies.pdf)

- (Ethercat, 2016) EtherCAT Technology Group , "EtherCAT vs. Modbus vs. Mechatrolink", 2016. Accessed on 21.5.2018. Available at: [http://www.ethercat.org/forms/taiwan2016/download/02\\_EtherCAT\\_vs\\_Modbus\\_vs\\_Mechatrolink\\_1609.pdf](http://www.ethercat.org/forms/taiwan2016/download/02_EtherCAT_vs_Modbus_vs_Mechatrolink_1609.pdf)
- (Ethercat, 2017a) Beckhoff Automation GmbH & Co., "ET1815, ET1816 | EtherCAT IP Core for Xilinx® FPGAs". Accessed on 28.11.2017. Available at: <https://www.ethercat.org/en/products/D798D576DED843AC83E87DDE1BDBCE54.htm>
- (Ethercat, 2017b) Beckhoff Automation GmbH & Co., "ET1810, ET1811, ET1812 | EtherCAT IP Core for Altera® FPGAs". Accessed on 28.11.2017. Available at: <https://www.ethercat.org/en/products/1002FBFAF6684D5D95896DDE625B461E.htm>
- (Etherlab, 2018) Etherlab, "Supported Ethernet Hardware", 2018. Accessed on 21.5.2018. Available at: <https://www.etherlab.org/en/ethercat/hardware.php>
- (Han & Song, 2003) Y. Han & Y. H. Song, "Condition Monitoring Techniques for Electrical Equipment—A Literature Survey", *IEEE Transactions on Power Delivery*, vol. 18, no. 1, pp. 4-13. Jan. 2003.
- (Jastrzebski et al., 2014) Jastrzebski et al., "Modelling and Evaluation of Radial-Axial PCB Capacitive Position Sensor Prototype", 2014. Accessed on 3.6.2018. Available at: <https://ieeexplore.ieee.org/document/6910956/>
- (Karmakar, 2016) Karmakar, S. et al., "Induction Motor Fault Diagnosis Approach through Current Signature Analysis". *Springer Singapore*, 2016. ISBN 978-981-10-0623-4.
- (Lantronix, 2016) Mouser Electronics, Lantronix PremierWave 2050 Enterprise Wi-Fi IoT Module Datasheet, 2016. Cited on 15.11.2017. Available at: [http://www.mouser.com/ds/2/224/910-817a\\_PW2050\\_DS\\_release-890475.pdf](http://www.mouser.com/ds/2/224/910-817a_PW2050_DS_release-890475.pdf)
- (Lindh, 2003) Lindh T, "On the Condition Monitoring of Induction Machines". *LUT printing press*, 2003. ISBN 951-764—841-3.
- (LUT, 2016) Lappeenranta University of Technology, "Electromagnetic Compatibility in Power Electronics", Lecture Slides, 2016.

- (MathWorks, 2017a) MathWorks, FIR Filter Design documentation webpage. 2017. Accessed on 17.11.2017. Available at: <https://se.mathworks.com/help/signal/ug/fir-filter-design.html#f4-9960>
- (MathWorks, 2017b) MathWorks, IIR Filter Design documentation webpage. 2017. Accessed on 17.11.2017. Available at: <https://se.mathworks.com/help/signal/ug/iir-filter-design.html>
- (National Instruments, 2016) National Instruments, "Sensors for Condition Monitoring", 2016. Accessed on 8.1.2018. Available at: <http://www.ni.com/white-paper/52461/en/>
- (Niskanen, 2014) Niskanen, V., "Radio-Frequency-Based Measurement Methods for Bearing Current Analysis in Induction Motors", *LUT printing press*, 2014. ISBN 978-952-265-728-2.
- (NTN, 2010) NTN Bearing Corporation, "Bearing Frequencies". Accessed on 21.5.2018. Available at: <http://www.ntnamericas.com/en/website/documents/brochures-and-literature/tech-sheets-and-supplements/frequencies.pdf>
- (PSK 5721) PSK Standards Association, "Vibration Measurements in Condition Monitoring. Measurement Settings", 2013.
- (Rao, 2000) J.S. Rao, "Vibratory Condition Monitoring of Machines". *Alpha Science International*, 2000. ISBN 1-84265-010-6.
- (Simatran, 2015) Simatrang, S., "Fault Detection for Rolling Element Bearings Using Model-Based Technique. Accessed on 21.5.2018. Available at: [https://etd.ohiolink.edu!etd.send\\_file?accession=case1436533779&disposition=inline](https://etd.ohiolink.edu!etd.send_file?accession=case1436533779&disposition=inline)
- (SKF, 2016) SKF Group, "SKF Vibration Sensors Catalog", 2016. Accessed on 5.10.2017. Available at: <http://www.skf.com/binary/49-267858/CM-P1-11604-14-EN-Vibration-Sensor-Catalog.pdf>
- (SOEM, 2015) Open EtherCAT Society, "Simple Open EtherCAT Master or SOEM", 2015. Accessed on 21.5.2018. Available at: <http://openethercatsociety.github.io/doc/soem/index.html>
- (Softing, 2017) Softing Industrial Automation GmbH, "EtherCAT Slave for Altera FPGA". Accessed on 29.11.2017. Available at:

<https://industrial.softing.com/en/products/embedded-solutions/protocol-stacks-for-fpgas/ethernetcat/ethernetcat-slave-for-altera-fpga.html>

- (Stamboliska, 2015) Zhaklina S. et al., "Proactive Condition Monitoring of Low-Speed Machines". *Springer International*, 2015. ISBN 978-3-319-10493-5.
- (Tavner, 1987) Tavner, P., Penman J., "Condition Monitoring of Electrical Machines", *Research studies press Ltd, England*, 1987. ISBN 0-86380-061-0.
- (Tavner, 2008) Tavner, P., Ran L., Penman J. and Sedding, H., "Condition Monitoring of Rotating Electrical Machines". *The Institution of Engineering and Technology*, 2008. ISBN 978-0-86341-739-9.
- (Texas Instruments, 2003a) Texas Instruments, XTR115 Current Loop Transmitter datasheet. Accessed on 15.11.2017. Available at: <http://www.ti.com/lit/ds/symlink/xtr115.pdf>
- (Texas Instruments, 2003b) Texas Instruments, "Combining the ADS1202 with an FPGA Digital Filter for Current Measurement in Motor Control Applications", 2003. Accessed on 19.11.2017. Available at: <http://www.ti.com/lit/an/sbaa094/sbaa094.pdf>
- (Texas Instruments, 2008) Texas Instruments, ADS1203 Delta-Sigma modulator datasheet, 2008. Accessed on 2.11.2017. Available at: <http://www.ti.com/lit/ds/symlink/ads1203.pdf>
- (Texas Instruments, 2017a) Texas Instruments, LMT01-Q1 temperature sensor datasheet, 2017. Accessed on 21.5.2018. Available at: <http://www.ti.com/lit/ds/snis192b/snis192b.pdf>
- (Texas Instruments, 2017b) Texas Instruments, "Digital Filter Types in Delta-Sigma ADCs", Application Report, 2017. Accessed on 21.5.2018. Available at: <http://www.ti.com/lit/an/sbaa230/sbaa230.pdf>
- (Texas Instruments, 2017c) Texas Instruments, "C2000™ Delfino™ 32-bit microcontrollers". Accessed on 21.5.2018. Available at: <http://www.ti.com/microcontrollers/c2000-performance-mcus/real-time-control/delfino-f2833x-f2837x/overview.html>
- (Texas Instruments, 2017d) Texas Instruments, "EtherCAT Interface for High Performance MCU Reference Design", 2017. Accessed on 21.5.2018. Available at: <http://www.ti.com/tool/TIDM-DELFINO-ETHERCAT>

(Tolsa, 2017) E-mail conversation with LUT capacitive sensor RF designer Tolsa, K., 2017.

## APPENDIX I I/II CIC COMPILER PARAMETERS

CIC Compiler 2.0 (Xilinx CIC Compiler 2.0)

Filter Specification | Implementation

Filter Specification

Filter Type: Decimation

Number of Stages: 3

Differential Delay: 1

Number of Channels: 1

Sample Rate Change Specification

Fixed  Programmable

Fixed or Initial Rate: 256

Minimum Rate: 256

Maximum Rate: 256

Hardware Oversampling Specification

Select format: Sample\_Period

Sample period: 1

Hardware Oversampling Rate: 1

OK Cancel Help Apply

## APPENDIX I II/II CIC COMPILER PARAMETERS

The image shows a screenshot of the Xilinx CIC Compiler 2.0 software interface, specifically the Implementation tab. The window title is "CIC Compiler 2.0 (Xilinx CIC Compiler 2.0)". The interface is divided into several sections:

- Numerical Precision:** This section contains a "Quantization:" label with two radio buttons: "Full\_Precision" (which is selected) and "Truncation". Below this is a text input field for "Output Data Width" with the value "42".
- Optional:** This section contains two checked checkboxes: "Use Xtreme DSP Slice" and "Use Streaming Interface".
- Control Options:** This section contains two unchecked checkboxes: "rst" and "en".
- FPGA Area Estimation:** This section contains an unchecked checkbox "Define FPGA area for resource estimation". Below it is a text input field for "FPGA area [slices, FFs, BRAMs, LUTs, IOBs, emb. mults, TBUFs]" with the value "[0,0,0,0,0,0,0]".

At the bottom of the window, there are four buttons: "OK", "Cancel", "Help", and "Apply".

## APPENDIX II DIGITAL FILTER DESIGN CODE

```
rp = 0.05;           % Passband ripple
rs = 60;            % Stopband ripple
fs = 20000;        % Sampling frequency
f = [3000 3500];   % Cutoff frequencies
a = [1 0];         % Desired amplitudes
dev = [(10^(rp/20)-1)/(10^(rp/20)+1) 10^(-rs/20)];
[n,fo,ao,w] = firpmord(f,a,dev,fs);
b = firpm(n,fo,ao,w);
fvtool(b)
freqz(b,1,1024,fs)
title('Lowpass Filter 3kHz')
```

## APPENDIX III MATLAB CODE USED IN FFT

```
%% 50 Hz
clc; clear all; close all;
X = importdata('50HZ_y.CSV',';');
Y = importdata('50HZ_x.CSV',';');

% Find when value != 0
i = findNotZero(X); % Remove initial zero values due to CM579 settling
X = X(i:length(X));
Y = Y(i:length(X));
tx = 1:1:length(X);
ty = 1:1:length(Y);
X50HZ = ((X-mean(X)) .* 0.3389); % Remove offset bias and scale to  $\mu\text{m}$ 
Y50HZ = ((Y-mean(Y)) .* 0.4042);

figure;
plot(tx,X50HZ,'b')
figure;
plot(ty,Y50HZ,'r')
figure;
plot(X(1:3000),Y(1:3000))

L = length(Y); % Length of signal
Yfft = fft(Y50HZ,L)
Fs = 20000; % Sampling frequency
T = 1/Fs; % Sampling period
t = (0:L-1)*T; % Time vector
wlen = 1000; % X-axis length
figure
P2 = abs(Yfft/L);
P1 = P2(1:L/2+1);
P1(2:end-1) = 2*P1(2:end-1);
f = Fs*(0:(L/2))/L

subplot(2,1,1)
plot(t,Y50HZ,'r');
ylabel('Displacement [ $\mu\text{m}$ ]');
xlim([0 1/5]); xlabel('Time [s]')
title('Signal, f_e_1 = 50 Hz, pp = 4')
grid minor;

subplot(2,1,2)
plot(f,P1,'r')
title('FFT Y-axis')
xlabel('f (Hz)')
ylabel('[Y(f)]')
grid minor;
```